Title

Global perturbation of the marine calcium cycle during the Permian-Triassic transition

Journal

Geological Society of America Bulletin, 130(7-8)

ISSN

0016-7606

Authors

Silva-Tamayo, Juan Carlos
Lau, Kimberly V
Jost, Adam B
et al.

Publication Date

2018-07-01

DOI

10.1130/b31818.1

Peer reviewed

Global perturbation of the marine calcium cycle during the Permian-Triassic transition

Juan Carlos Silva-Tamayo, Kimberly V. Lau, Adam B. Jost, Jonathan L. Payne, Paul B. Wignall, Robert J. Newton, Anton Eisenhauer, Donald J. Depaolo, Shaun Brown, Kate Maher, Daniel J. Lehrmann, Demir Altiner, Meiyi Yu, Sylvain Richoz, and Adina Paytan

Abstract

A negative shift in the calcium isotopic composition of marine carbonate rocks spanning the end-Permian extinction horizon in South China has been used to argue for an ocean acidification event coincident with mass extinction. This interpretation has proven controversial, both because the excursion has not been demonstrated across multiple, widely separated localities, and because modeling results of coupled carbon and calcium isotope records illustrate that calcium cycle imbalances alone cannot account for the full magnitude of the isotope excursion. Here, we further test potential controls on the Permian-Triassic calcium isotope record by measuring calcium isotope ratios from shallow-marine carbonate successions spanning the Permian-Triassic boundary in Turkey, Italy, and Oman. All measured sections display negative shifts in $\delta^{44/40}Ca$ of up to 0.6‰. Consistency in the direction, magnitude, and timing of the calcium isotope excursion across these widely separated localities implies a primary and global $\delta^{44/40}Ca$ signature. Based on the results of a coupled box model of the geological carbon and calcium cycles, we interpret the excursion to reflect a series of consequences arising from volcanic CO_2 release, including a temporary decrease in seawater $\delta^{44/40}Ca$ due to short-lived ocean acidification and a more protracted increase in calcium isotope fractionation associated with a shift toward more primary aragonite in the sediment and, potentially, subsequently elevated carbonate saturation states caused by the persistence of elevated CO_2delivery from volcanism. Locally, changing balances between aragonite and calcite production are sufficient to account for the calcium isotope excursions, but this effect alone does not explain the globally observed negative excursion in the $\delta^{13}C$ values of carbonate sediments and organic matter as well. Only a carbon release event and related geochemical consequences are consistent both with calcium and carbon isotope data. The carbon release scenario can also account for oxygen isotope evidence for dramatic and protracted global warming as well as paleontological evidence for the preferential extinction of marine animals most susceptible to acidification, warming, and anoxia.

INTRODUCTION

The Late Permian to Early Triassic transition spans the most severe environmental and biological crisis of the Phanerozoic (e.g., Erwin, 1994; Wignall and Twitchett, 1996; Erwin et al., 2002; Payne and Clapham, 2012). Negative excursions in the carbon isotope ($\delta^{13}C$) values of carbonate

rocks and organic matter in Upper Permian–Lower Triassic sedimentary sequences (reviewed in Korte and Kozur, 2010) suggest that the mass extinction event was associated with a major perturbation of the exogenic carbon cycle. However, the source and amount of carbon released and its impact on surface environments cannot be constrained via carbon isotope data alone (Berner, 2002; Payne et al., 2010).

The geological carbon cycle is coupled to the geological calcium cycle via the weathering and deposition of carbonate rocks. Because calcium isotopes ($\delta^{44/40}Ca$) in carbonate sediments are fractionated relative to calcium in seawater, imbalances in the rates of calcium delivery to the oceans relative to calcium removal in sediments can affect seawater $\delta^{44/40}Ca$ (e.g., Fantle, 2010). Therefore, calcium isotopes hold potential for further quantification of the nature of the Permian-Triassic global change (Fantle, 2010; Payne et al., 2010; Fantle and Tipper, 2014; Komar and Zeebe, 2016). To date, there exist three high-resolution calcium isotope records spanning the Permian-Triassic transition (late Changhsingian–early Griesbachian), two measured in shallow-marine limestones from South China and Turkey, and one measured on conodont microfossils (Figs. 1–3; Payne et al., 2010; Hinojosa et al., 2012; Lau et al., 2017). Each record exhibits a negative excursion in $\delta^{44/40}Ca$ values across the Changhsingian-Griesbachian transition lasting ~500 k.y., which has previously been interpreted to reflect variation in the $\delta^{44/40}Ca$ values of seawater during that time (Payne et al., 2010; Hinojosa et al., 2012).

Payne et al. (2010) used a forward box model of the marine calcium cycle to argue that the negative excursion in $\delta^{44/40}Ca$ of marine carbonate sediments resulted from an interval of reduced carbonate production during a transient ocean acidification event combined with increased continental weathering, each of which was in turn caused by the rapid release of volcanic CO_2 to the atmosphere (10,000–50,000 petagrams [Pg] of carbon). Komar and Zeebe (2016) used a coupled model of the geological carbon and calcium cycles to argue that ocean acidification could not have been the only mechanism responsible for the negative excursion in $\delta^{44/40}Ca$. These authors suggested that the magnitude of the negative excursion in the $\delta^{44/40}Ca$ record from limestones also requires an increase in the Ca isotope fractionation between calcite and seawater. They proposed that this increase in Ca isotope fractionation resulted from a decrease in oceanic carbonate saturation, which in turn resulted from lower productivity and a weaker biological pump. Their model assumes that the fractionation between seawater and carbonate sediments becomes larger at lower precipitation rates, based on work by Gussone et al. (2005) and Lemarchand et al. (2004). However, this relationship is inconsistent with (and opposite in direction to) theoretical (DePaolo, 2011; Nielsen et al., 2012) and other experimental results (Tang et al., 2008; Watkins et al., 2017), observations of pore fluids and sediments in deep-sea cores (Fantle and DePaolo, 2007), and calcium in freshwater aquifers (Jacobson and Holmden, 2008).

As illustrated by these diverging interpretations, better understanding of the controls underlying the $\delta^{44/40}Ca$ excursion in the carbonate rock record is challenging for several reasons. First, there are a small number of $\delta^{44/40}Ca$ records, with limited geographic coverage. This paucity of data makes it difficult to rule out local factors such as spatial variation in $\delta^{44/40}Ca$ values of seawater or diagenetic influences specific to South China as alternative explanations for the negative shift in $\delta^{44/40}Ca$ at the Permian-Triassic transition (e.g., Lau et al., 2017). Second, the modeling approaches employed in previous studies included scenarios that can now be better constrained with experimental and theoretical data, including the effects of precipitation rate and changing proportions of aragonite versus calcite in marine sediments.

Additional calcium isotope records from widely spaced stratigraphic sections located on other continental margins are critical for testing the primary, global nature of the negative calcium isotope signature. To address this need, we measured the calcium isotope compositions of marine carbonate strata spanning the Upper Permian to Lower Triassic transition (uppermost Changhsingian to lowermost Griesbachian) at the Tesero Road section in the Dolomite Mountains of northern Italy and at the Saiq Plateau section in the Sultanate of Oman (Figs. 4–5). Thus, our combined data set includes high-resolution records from five geographic areas and both carbonate rocks and conodont elements. We use coupled forward box models of the marine calcium and carbon cycles to assess the potential isotopic effects of rapid volcanic CO_2outgassing, changes in ocean alkalinity and phosphate, and changes in the dominant carbonate mineralogy on the calcium and carbon isotope composition of seawater during latest Changhsingian through Griesbachian time.

STRATIGRAPHY AND AGE OF THE STUDIED SUCCESSIONS

The only published calcium isotope data spanning the Permian-Triassic boundary (PTB) in carbonate rocks come from the Dajiang section in the Great Bank of Guizhou, Nanpanjiang Basin, South China (Figs. 1 and 2; Payne et al., 2010) and the Taşkent section in the Taurus Mountains of southern Turkey (Fig. 3; Lau et al., 2017). For this study, we collected samples along measured stratigraphic sections from the Saiq Plateau section, Al Jabal Al-Akhdar, Sultanate of Oman, and the Tesero Road section in the Dolomite Mountains of northern Italy. (Figs. 4 and 5). The depositional ages of the studied strata have been determined using conodont and foraminiferan biostratigraphy (Perri, 1991; Farabegoli and Perri, 1998; Perri and Farabegoli, 2003; Groves et al., 2005; Groves and Altiner, 2005) and by carbon isotope chemostratigraphic correlation to the global stratotype section and point (GSSP) at Meishan, China (Fig. 6), for which high-precision radiometric dates are available (Shen et al., 2011; Burgess et al., 2014).The uppermost Changhsingian–lowermost Griesbachian carbonates at the Tesero section belong to the Bellerophon and Werfen Formations (Wignall and Hallam, 1992). The section (Fig. 4) consists of Changhsingian dolomicrites capped by

a thin bed of bioclastic packstone belonging to the Bellerophon Formation, followed by alternating oosparites and micrites (the Tesero oolite horizon of the Werfen Formation) deposited at shallow depths on a carbonate ramp located along the western limit of the Tethys Ocean (Wignall and Hallam, 1992; Brandner et al., 2012). Carbon isotope stratigraphy (Fig. 4) and fossil occurrences indicate that the end-Permian mass extinction horizon occurs within the basal 3–4 m of the Tesero oolite horizon and that the PTB occurs a few meters higher (Figs. 2 and 5; Perri, 1991; Wignall and Hallam, 1992; Wignall and Twitchett, 1996). The Tesero oolite horizon is overlain by a series of lower Griesbachian pyritic marls and micrites, which are in turn overlain by series of upper Griesbachian ostracod packstones of the Mazzin Member of the Werfen Formation (Fig. 4). The lower *Isarcicella isarcica*conodont zone occurs within the basal 2 m of the Mazzin Member (Fig. 4; Perri, 1991; Perri and Farabegoli, 2003).

The studied Upper Permian–Lower Triassic carbonate succession from the Saiq Plateau section, Al Jabal Al-Akhdar, Sultanate of Oman, belongs to the Saiq Formation (Koehrer et al., 2010; Baud and Richoz, 2013; Richoz et al., 2014). Deposition of the Saiq Formation carbonate successions occurred on an extensive tropical carbonate platform that covered most of the modern Arabian Peninsula (Koehrer et al., 2010; Richoz et al., 2010a). This platform developed during the Middle Permian following the rifting phase that pulled apart the Cimmerian terranes from the Gondwana continent (Richoz et al., 2014). The Saiq Formation consists mainly of dolostones. The Upper Permian (Changhsingian) carbonate succession belongs to Unit B (Richoz et al., 2010b, 2014) and consists of fossiliferous dolopackstones/dolowackestones, with a few intercalated strata of framestones/boundstones (Fig. 5). The end-Permian mass extinction horizon is in the upper part of the dolopackstones of Unit B, just below a 1-m-thick intraformational breccia, which sits on a small disconformity. This disconformity is not likely to represent a long interval of time, based on the presence of the negative carbon isotope excursion (Figs. 5 and 6). The PTB occurs at the first minimum of the negative carbon isotope excursion, 2 m above the extinction level (Richoz et al., 2010b). The Changhsingian Unit B is overlain by the Griesbachian Unit C of the Saiq Formation, which consists of a basal fossiliferous grainstone and a series of intercalated dolomudstones and dolowackestones overlain by a 5–8-m-thick polymict breccia (Fig. 5). Because the conodont *Hindeodus parvus* has not yet been found in this section, the presence or absence of the time represented by the *H. parvus* conodont zone cannot currently be determined. The absence of the *H. parvus* conodont zone may be related to erosion associated with the formation of the intraformational breccia from the base of Unit C. Alternatively, its absence could be related to the relatively low abundance of conodonts in this stratigraphic section, likely relating to the depositional environment. The later *I. isarcica* conodont zone begins at the base of the lower fossiliferous dolograinstone at the base of Unit C.

The studied strata in the Taşkent section belong to the Çekiç Dağ and Gevne Formations (Ünal et al., 2003; Richoz, 2004; Payne et al., 2007; Pruss et al., 2006). The Upper Permian (Changhsingian) Çekiç Dağ Formation (Fig. 3) consists mainly of subtidal, open-marine, fossiliferous wackestones and packstones deposited on a ramp located on the western margin of the Tethys Ocean (Groves et al., 2005; Payne et al., 2007). An oolitic grainstone horizon marks the top of the Çekiç Dağ Formation and is overlain by a 1–3-m-thick interval of stromatolitic microbialite at the base of the Gevne Formation. The microbialite is followed by thin-bedded micritic limestone, thicker-bedded oolitic grainstones, and fine-grained siliciclastic strata (Fig. 3). Carbon isotope stratigraphy (this work; Lau et al., 2016) and foraminiferan biostratigraphy (Richoz, 2004; Groves et al., 2005) indicate that the end-Permian mass extinction horizon and biostratigraphic PTB correlate to the basal centimeters of the oolitic grainstone at the top of the Çekiç Dağ Formation and the base of the overlying stromatolitic beds, respectively (Fig. 4). The occurrence of the conodont *H. parvus* at the correlative Curuk Dağ section in Turkey (Crasquin-Soleau et al., 2002) is consistent with this interpretation. The inferred position of the *I. isarcica* conodont zone is based on carbon isotope chemostratigraphic correlation to bed 28 at the Meishan section, China (Fig. 3).

Carbonates from the Dajiang section in the Great Bank of Guizhou, an isolated carbonate platform in the Nanpanjiang Basin, South China (Fig. 2), belong to the fossiliferous Upper Permian Wujiaping Formation and to an overlying microbialite interval, which is ~16 m thick, followed by 60 m of thin-bedded, micritic carbonates belonging to the Lower Triassic Daye Formation (Lehrmann et al., 1998, 2006). These strata were deposited in a shallow-marine environment in the interior of the Great Bank of Guizhou, which initiated on top of a paleotopographic high on the Yangtze Platform during latest Permian and earliest Triassic time (Lehrmann et al., 1998). The Great Bank of Guizhou was an isolated carbonate platform located in the eastern limits of the Tethys Ocean (Lehrmann et al., 1998). Carbon isotope chemostratigraphy and conodont biostratigraphy (Fig. 2) suggest that the end-Permian mass extinction horizon occurs at the contact between the uppermost wackestones of the Wujiaping Formation and the overlying microbialite of the Daye Formation. The PTB, based on the first occurrence of *H. parvus*, is within the microbialite interval, ~8 m above the contact with the Wujiaping Formation (Chen et al., 2009). In this section, the *I. isarcica*conodont zone, and therefore extinction pulse 2 (EP2) of Song et al. (2012), occurs above the microbialite interval, within the basal 4 m of the Daye Formation (Figs. 2 and 6).

METHODS

We performed calcium isotope measurements on carbonates from the Taşkent and Saiq Plateau sections at the mass spectrometer facilities of GEOMAR, Helmholtz Centre for Ocean Research, Kiel, Germany, following the methods described in Heuser et al. (2002), Böhm et al. (2006), and Farkaš et

al. (2007a, 2007b). Briefly, polished slabs of the carbonate samples were drilled using a 1 mm bit to sample micrite and to minimize sampling of biogenic and secondary carbonate facies. Powdered samples from Oman were dissolved in 2 *N* HCl. A fraction of the solution was spiked with a $^{43}Ca/^{48}Ca$ double spike and loaded onto a Biorad AGW 50X8, 200–400 mesh resin, following the methods described by Heuser et al. (2002), for purification (separation) of Ca^{2+} from other cations. The purified calcium fraction was evaporated to dryness and redissolved in 2 *N* HCl and loaded with a $TaCl_5$ activator on a single zone-refined Re filament for mass spectrometric analyses in a Thermo Fisher Triton thermal ionization mass spectrometer (TIMS; Farkaš et al., 2007a, 2007b). All samples were analyzed at least three times. The calcium isotope compositions are reported using delta notation ($\delta^{44/40}Ca$, ‰) relative to the National Institute of Standards and Technology (NIST) standard SRM 915a (Hippler et al., 2003). The external reproducibility was better than 0.1‰ (2 standard deviation) for most of the samples. Replicate isotope analyses of the GEOMAR-Kiel in-house CaF_2 standard yielded average $\delta^{44/40}Ca_{(SRM\ 915a)} = 1.4‰$, with $2\sigma_{mean} = 0.1‰$, in agreement with previously published values (Hippler et al., 2003). Aliquots of the NIST SRM 915a standard were also subjected to all the wet chemistry preparation steps performed on the carbonate samples. The NIST standard SRM 915a yielded $\delta^{44/40}Ca_{(SRM\ 915a)} = 0.0‰$, $2\sigma_{mean} = 0.1‰$.

Samples from the Tesero Road sections were analyzed at the Center for Isotope Geochemistry, University of California, Berkeley, California, following Jost et al. (2017). The drilled samples were dissolved in 1 *N* acetic acid. A fraction of the solution was spiked with a $^{42}Ca/^{48}Ca$ double spike, evaporated to dryness, redissolved in HNO_3, and loaded onto element-specific resin (DGA Eichrom Technologies) for chromatographic calcium purification. A fraction of purified calcium was loaded on a Re filament with 3 *M* HNO_3 and ~0.25 µL phosphoric acid (H_3PO_4). Mass spectrometric analyses were performed using a Thermo Fisher Triton multicollector TIMS. Samples were analyzed at least three times. The calcium isotope compositions are reported using delta notation ($\delta^{44/40}Ca$, ‰) against the NIST standard SRM 915a (Hippler et al., 2003). The NIST standard SRM 915a yielded $\delta^{44/40}Ca_{(SRM\ 915a)} = 0.1‰$, $2\sigma_{mean} = 0.1‰$.

The carbon and oxygen isotope analyses of the carbonate samples from the Saiq Plateau section were performed at Graz University using a Finnigan Kiel II carbonate device coupled to a Thermo Finnigan Delta Plus isotope ratio mass spectrometer following the methods described by Clarkson et al. (2013). The carbon and oxygen isotope results are presented using delta notation, normalized against the international Vienna Peedee belemnite (V-PDB) standard. The oxygen isotope compositions of dolomite samples were corrected for the difference in fractionation between calcite and dolomite following Vasconcelos et al. (2005). The carbon and oxygen isotope data for the samples from the Tesero Road section, the Dajiang section, and the

Taşkent section have been reported previously (Newton et al., 2004; Payne et al., 2010; Lau et al., 2016, 2017).

The elemental compositions of the carbonates from the Tesero Road and Saiq Plateau sections were determined on the same aliquots used for calcium isotope determinations. Samples were dissolved in 1% acetic acid, dried, and redissolved in 3% nitric acid. The solutions were analyzed using an inductively coupled plasma–optical emission spectrometer. The analytical error of replicate standard analyses was better than 0.1% for major and 0.0001% for minor elements.

RESULTS

Carbon and Oxygen Isotopes

The widely recognized negative $\delta^{13}C$ excursion at the PTB was also observed at the Tesero Road section (Fig. 4; Table DR1[1]), where $\delta^{13}C$ values decrease from +4.0‰ in the upper Changhsingian to –4.0‰ at the *I. isarcica* datum. Because the overlying limestone is poorly exposed, sampling of the Lower Triassic is scarce; however, our data show a return to 1‰ by 92 m.

The $\delta^{13}C$ chemostratigraphy of the Saiq Formation confirms the drop in the $\delta^{13}C$ values reported by Richoz et al. (2010a, 2010b), from +5.6‰ to +1.3‰ from the upper Changhsingian to the main end-Permian extinction horizon (Fig. 5). The $\delta^{13}C$ values further decrease to +0.8‰ in the lowermost Triassic (Richoz et al., 2010a). The values increase to +3.0‰ toward the middle Griesbachian and are around +2.5‰ in the upper Griesbachian.

Our measurements confirm the existence of a large negative excursion in the $\delta^{13}C$ record of limestone in multiple shallow-marine locations. The overall pattern of isotope variation at Tesero Road (Fig. 4; Newton et al., 2004) and in the Saiq Formation (Fig. 5) closely resembles that of the Taşkent section in Turkey (Fig. 3; Lau et al., 2017), the Dajiang section of South China (Fig. 2; Payne et al., 2010), and many other sites (cf. Korte et al., 2004; Korte and Kozur, 2010).

The $\delta^{18}O$ values of the Tesero Road section vary between –5.3‰ and –7.3‰, with the exception of two values that reached –1.8‰ and –2.8‰ immediately below the extinction horizon (Table DR1 [see footnote 1]; Newton et al., 2004). The $\delta^{18}O$ values of Changhsingian carbonates from the Saiq Plateau section range between –3.8‰ to –2.5‰ below the extinction horizon. Above the extinction horizon, $\delta^{18}O$ increases to –1.0‰ in the middle Griesbachian and then decreases again to –2.7‰ in the upper Griesbachian. These dolomite values fall within the range of values displayed by other dolomite successions in Oman and Iran (Clarkson et al., 2013). The Changhsingian carbonates from the Taşkent section have $\delta^{18}O$ values between –5.0‰ and –6.0‰, whereas the $\delta^{18}O$ values in the Griesbachian carbonates decrease to between –6.0‰ and –8.0‰ (Table DR1 [see footnote 1]).

Calcium Isotopes

Figures 2–4 illustrate the calcium isotope composition of carbonate rocks from the studied localities. The lowermost Changhsingian wackestones and mudstones from the Tesero Road section display $\delta^{44/40}$Ca values around +0.3‰ (Fig. 2). These $\delta^{44/40}$Ca values decrease to ~0‰ at the onset of the mass extinction and fluctuate between 0‰ and +0.2‰ in the latest Changhsingian Tesero oolite horizon (Fig. 4). The $\delta^{44/40}$Ca values of approximately +0.2‰ occur in both mudstones and oolites from the Griesbachian part of the Mazzin Member (Werfen Formation). Higher in the section, the $\delta^{44/40}$Ca values decrease to 0‰ in the Mazzin Member before increasing to +0.2‰ in the *I. isarcica* conodont zone (Fig. 4). The $\delta^{44/40}$Ca values decrease to 0‰ in the overlying oolitic packstones of the Griesbachian Mazzin Member.

Carbonates from the lower interval of the Changhsingian wackestone from the Saiq Plateau section display $\delta^{44/40}$Ca values between +0.6‰ and +0.8‰ (Fig. 5). These values increase up in the stratigraphy and reach +1.2‰ at the base of the coral- and crinoid-rich interval and then decrease to +0.6‰ in the packstone underlying the extinction horizon. The $\delta^{44/40}$Ca values further decrease to +0.4‰ in the lower Griesbachian breccias but then increase gradually to values between +0.9‰ and +1.2‰ in the middle to upper Griesbachian packstones (Fig. 5).

The $\delta^{44/40}$Ca of Changhsingian wackestones from the Çekiç Dağ Formation at Taşkent was reported by Lau et al. (2017) and is summarized here. The $\delta^{44/40}$Ca values shift from background values near +0.6‰ (the lowermost sample of the wackestone succession) to values near +0.1‰ a few meters below the main extinction horizon (Fig. 3; Table DR1 [see footnote 1]). The $\delta^{44/40}$Ca values of the upper Çekiç Dağ Formation range between 0.0‰ and +0.3‰ and then drop to 0.0‰ at the oolite unit containing the main end-Permian extinction horizon. Carbonates from the uppermost part of the oolite of the Changhsingian-aged Çekiç Dağ Formation have $\delta^{44/40}$Ca values near +0.3‰, which are interrupted by a drop to values as low as 0.0‰ in the lower microbialite of the lower Griesbachian Gevne Formation (Fig. 3). The upper part of the lower Griesbachian microbialite displays a rapid positive shift in $\delta^{44/40}$Ca values to +0.4‰ in the *I. isarcica* conodont zone. The $\delta^{44/40}$Ca values decrease again to 0.1‰ and remain low within the lower intercalated mudstone-wackestone of the Gevne Formation and part of its overlying oolitic packstone (Fig. 3). The light $\delta^{44/40}$Ca values are interrupted by a shift toward more positive values near +0.6‰ and then vary between +0.6‰ and +0.8% in the middle Griesbachian.

The δ^{13}C stratigraphy of the Dajiang section (Fig. 2) has been reported elsewhere (Payne et al., 2010), and the biostratigraphy has been evaluated in detail by Jiang et al. (2014). Briefly, the oldest Changhsingian carbonates (wackestones) display $\delta^{44/40}$Ca values between +0.4‰ and +0.7‰ (Fig. 2). Those values decrease to +0.2‰ at the onset of the microbialites overlying

the extinction horizon. The $\delta^{44/40}Ca$ values increase again to +0.4‰ at the base of the overlying mudstones, coincident with the *I. isarcica* conodont zone. The $\delta^{44/40}Ca$ values then decrease up section to +0.1‰, followed by a shift toward values of +1.2‰ in the uppermost part of the lower Griesbachian mudstone, and they remain high within the overlying oolitic grainstone (Fig. 2).

Major and Trace Elements

Carbonates from the Tesero Road section contain variable [Sr], from a background near 90 ppm in the Changhsingian mudstone to values near 300 ppm in the Changhsingian packstones (Fig. 4; Table DR1 [see footnote 1]). The Sr concentrations then increase to values as high as 1586 ppm in the uppermost Changhsingian oolitic packstones. The [Sr] value decreases in the lower Griesbachian mudstones to values between 155 ppm and 335 ppm and then increases to values as high as 994 ppm in middle-upper Griesbachian grainstones (Fig. 4; Table DR1 [see footnote 1]). The Sr/Ca ratios fluctuate between 0.0003 and 0.0009 in the Changhsingian mudstones and packstone and then increase to values as high as 0.0030 in the latest Changhsingian oolitic grainstones. These values decrease to below 0.0010 in the lower Griesbachian mudstones and increase again to values as high as 0.0050 in the middle-upper Griesbachian grainstones (Fig. 4; Table DR1 [see footnote 1]). Mg/Ca ratios fluctuate between 0.01 and 0.50 in the Changhsingian mudstones and packstones. The Mg/Ca ratios of the overlying oolitic grainstones are <0.06. The middle-upper Griesbachian oolitic grainstones have Mg/Ca <0.01. The Mn/Sr ratios of the Changhsingian mudstone and packstone samples vary between 0.40 and 2.13, whereas those of their overlying oolitic grainstones are generally <0.70 (Table DR1 [see footnote 1]). The Griesbachian marls displays an increase in Mn/Sr values to ~4.0. The Mn/Sr values then decrease below 0.8 in the overlying oolitic grainstones (Table DR1 [see footnote 1]).

The [Sr] values of Changhsingian dolomites from the Saiq Plateau section are low and then increase up section from 18 to 57 ppm (Fig. 5; Table DR1 [see footnote 1]). The Sr/Ca ratio of these dolostones ranges between 0.0002 and 0.0003, the Mg/Ca ratio ranges between 0.89 and 0.95, and the Mn/Sr ratio ranges between 2.7 and 3.2 (Fig. 5; Table DR1 [see footnote 1]). The [Sr] values of the lower Griesbachian dolostones increase up section from 53 ppb to 77 ppm, followed by a return to 54 ppm in the upper Griesbachian dolostones. The Sr/Ca ratios are usually below 0.0002, the Mg/Ca ratios vary between 0.90 and 0.92, and the Mn/Sr ratios vary between 2.7 and 3.0 (Fig. 5; Table DR1 [see footnote 1]).

Carbonates from the Taşkent section exhibit an increase in [Sr] value from a background near 700 ppm in the Changhsingian up to 3780 ppm in the lower Griesbachian (Fig. 3; Table DR1 [see footnote 1]). These values decrease to 1100 ppm and fluctuate between 1550 and 2000 ppm in the middle-upper Griesbachian. Variations in [Sr] values are paralleled by variations in the

Sr/Ca and Mg/Ca values (Fig. 3; Table DR1 [see footnote 1]). The Changhsingian–lower Griesbachian carbonates display Mn/Sr ratios that are predominantly <0.1. The middle-upper Griesbachian carbonates display slightly higher Mn/Sr values, between 0.1 and 0.4 (Table DR1 [see footnote 1]).

Carbonates from the Dajiang section display increasing [Sr] values from a background of 432 ppm in the Changhsingian to a maximum of 1451 ppm in the lower Griesbachian (Fig. 2; Table DR1 [see footnote 1]). These values decrease to 271 ppm in the lower-middle Griesbachian. The Sr/Ca values range between 0.0010 and 0.0040 and parallel the evolution of the [Sr] values. The Mg/Ca values fluctuate between 0.02 and 0.10, with exception of two middle Griesbachian samples with high Mg/Ca values ~0.5 (Fig. 2; Table DR1 [see footnote 1]). The Mn/Sr values vary between 0.1 and 0.3 in the upper Changhsingian packstones and vary between 0.4 and 2.5 in the overlying Changhsingian–Griesbachian microbialite. Those values decrease below 0.3 in the overlying Griesbachian mudstones and the middle-upper Griesbachian oolitic grainstones (Table DR1 [see footnote 1]).

DISCUSSION

Preservation of a Global Marine Sedimentary Calcium Isotope Signal

Based on the biostratigraphic and carbon isotope chemostratigraphic correlation of the studied successions, similar stratigraphic patterns in the carbonate sediment $\delta^{44/40}Ca$ values are apparent in the Dajiang and Taşkent sections (Fig. 6), with both sections exhibiting $\delta^{44/40}Ca$ minima near the Permian-Triassic transition, albeit with a potentially earlier initiation at Taşkent than at Dajiang. Based on U-Pb geochronology for the Meishan PTB stratotype section (Burgess et al., 2014), the duration of the negative excursion in $\delta^{44/40}Ca$ across the PTB is ~500 k.y. The $\delta^{44/40}Ca$ values vary continuously and smoothly across facies transitions within sections and correspond well among widely separated stratigraphic sections with differing depositional facies and diagenetic histories. The similar stratigraphic trends of the carbonate $\delta^{44/40}Ca$ values appear to be independent of changes in depositional environment and suggest a primary sedimentary signature reflecting global controls, rather than postdepositional diagenetic resetting (e.g., Lau et al., 2017).

The two most important potential global controls on the $\delta^{44/40}Ca$ values of carbonate sediments are the $\delta^{44/40}Ca$ values of contemporaneous seawater and the fractionation factor associated with carbonate precipitation (Farkaš et al., 2007a; Blättler et al., 2012). To reconstruct the evolution of the seawater $\delta^{44/40}Ca$ record through time, one would ideally measure a carbonate phase with a known fractionation factor relative to seawater, as has been done using biogenic calcite across the Phanerozoic (Farkaš et al., 2007a). Due to the scarcity of well-preserved, macroscopic skeletal carbonates of known mineralogical composition in Lower Triassic strata, however, analysis in this study must be focused on the bulk micritic

component of the samples. Because skeletal carbonates are exceedingly rare in many Lower Triassic carbonate sections, much less than 1% of sediment volume at Dajiang (Payne et al., 2006b) for example, it is implausible that a significant fraction of the micrite was produced by the comminution of larger biological grains produced under strong enzymatic control. More likely sources of the micrite in these sections are direct production in the marine water column as whitings, either induced in association with plankton blooms or produced through simple abiotic nucleation, and biologically induced precipitation associated with microbial mats on the seafloor (Payne et al., 2006b). The precise origins of the studied micrite are impossible to ascertain, but abiotic and biologically induced precipitates are more likely to exhibit precipitation rates that correlate with the carbonate saturation state of ambient seawater than are enzymatically controlled skeletal carbonates, and they are more likely to potentially vary in mineralogy in relationship to seawater temperature or Mg/Ca (Balthasar and Cusack, 2015). The presence of other primary, abiotic carbonate phases such as ooids, some quite large (Payne et al., 2006a; Tian et al., 2015; Lehrmann et al., 2012), and seafloor aragonite fans (e.g., Payne et al., 2007) in many Lower Triassic carbonate sequences is consistent with high levels of carbonate saturation. For example, extrapolating from ooid growth experiments, Trower et al. (2017) suggested that centimeter-scale ooids require extremely high local carbonate saturation states (omega >> 6). Because biologically induced and abiotic carbonate sediments can vary in precipitation rate and mineralogy as well as in the value of $\delta^{44/40}Ca$, it is important to address the potential for each of these factors to have influenced the $\delta^{44/40}Ca$ values of micritic sediments spanning the PTB interval.

Seawater $\delta^{44/40}Ca$, precipitation rate, and original mineralogy are important potential controls on the $\delta^{44/40}Ca$ values of limestone. The controls on dolomite $\delta^{44/40}Ca$ are more complex, especially when it is secondary in origin. The Changhsingian-Griesbachian negative shift in carbonate $\delta^{44/40}Ca$ values is also displayed in dolomites from the Saiq Plateau section (Fig. 6). However, these dolomites have absolute $\delta^{44/40}Ca$ values up to 0.4‰ higher than those of correlative limestones. The effects of dolomitization on the sedimentary $\delta^{44/40}Ca$ composition of carbonates remain poorly understood, and contrasting hypotheses have been proposed regarding the potential effects of dolomitization on the carbonate $\delta^{44/40}Ca$ record. For instance, early dolomitization (i.e., dolomitization during which the source fluids are still ultimately derived from overlying seawater, such as through reflux brines, and in which the dolomitizing fluids may also be released back into seawater) could potentially increase the carbonate $\delta^{44/40}Ca$ values, because the light calcium isotopes are preferentially released from the carbonate lattice during the replacement of calcium (Heuser et al., 2005). A similar effect occurred in Neogene shallow-marine carbonates affected by dolomitization and long-lasting postdepositional marine diagenesis in the

presence of seawater (Fantle and Tipper, 2014; Fantle and Higgins, 2014). The preferential loss of ^{40}Ca during dolomitization could also reduce the stratigraphic variation in $\delta^{44/40}Ca$ of the remaining calcium within the dolomitized strata. Similarly, modern shallow-marine carbonates affected by early diagenesis have higher $\delta^{44/40}Ca$ and $\delta^{18}O$ values than those diagenetically unaffected (Fantle and Higgins, 2014). In contrast, Holmden et al. (2012) argued that postdepositional dolomitization of carbonates might result in low $\delta^{44/40}Ca$ values if ^{40}Ca-rich intrabasinal dolomitizing fluids derived from evaporitic brines interact with marine carbonates during burial. Silva-Tamayo et al. (2010a, 2010b) suggested, instead, that Neoproterozoic seawater calcium isotope composition is preserved by dolomitized carbonates and even by slightly metamorphosed dolomitic carbonates (e.g., Marinoan and Sturtian cap carbonates from central and northwestern Brazil), because they have $\delta^{44/40}Ca$ values like those of their correlative aragonitic carbonates from Canada and central and southwestern Brazil. The $\delta^{44/40}Ca$ values of dolomites from the Saiq Plateau correlate with geochemical indicators of diagenetic alteration ($\delta^{18}O$ and Mn/Sr; Fig. 7), and the $\delta^{18}O$ values of the Saiq dolomites are systematically heavier than those of their global correlatives (Fig. 7). Based on the elevated $\delta^{18}O$ and $\delta^{44/40}Ca$ values of the Saiq Plateau dolomites relative to coeval limestones in other sections, these isotope compositions are most consistent with alteration via the early diagenetic mechanisms proposed by Fantle and Higgins (2014), i.e., preferential early loss of ^{40}Ca during dolomitization.

The subsurface equivalent to the Saiq Formation, the Khuff Formation, experienced a complex diagenetic history with three periods of dolomitization, four phases of calcite cementation, and two periods of anhydrite cementation (Perez-Gomez et al., 2014). Petrographic and isotopic evidence indicates that the most dominant phase, early dolomite, formed during diagenetic alteration of the original limestone by shallow brines circulating in a reflux process (Perez-Gomez et al., 2014). This early dolomitization was confirmed by outcrop observations (Koehrer et al., 2010). Detailed oxygen isotopic study of these different phases showed that only dolomites precipitated through shallow brine circulation during early dolomitization have more positive values than co-occurring limestone, whereas dolomite formed during later diagenetic processes (deep burial dolomitization) display more negative values (Perez-Gomez et al., 2014). These observations are consistent with an interpretation that the high sedimentary $\delta^{44/40}Ca$ values of the Saiq Plateau dolomites resulted from early dolomitization of the carbonate system in association with the circulation of shallow brines.

The upper Griesbachian carbonates from the Dajiang section are also dolomitized and have Mg/Ca ratios close to 0.5 (Fig. 2; Table DR1 [see footnote 1]). The carbonates, which have been pervasively dolomitized during burial diagenesis (Lehrmann et al., 2012; Kelley et al., 2011), display $\delta^{44/40}Ca$ values that are ~0.2‰ higher than those of correlative limestones

from the Taşkent section but are 0.4‰ lower than those of their correlatives at the Saiq Plateau. These differences among sections suggest that dolomitization can modify the calcium isotope composition of carbonates differently depending on local factors such as the source and composition of the dolomitizing fluids, as well as the nature of their interactions with local sediments.

Global Calcium Cycle Dynamics during the Permian-Triassic Transition

In aggregate, the new $\delta^{44/40}Ca$ values from the limestone sections at Taşkent and Tesero Road indicate a temporary, global shift toward lighter values by several tenths of a permil across the end-Permian extinction interval, followed by a later excursion to heavier values (Fig. 6). To quantitatively explore the extent to which different scenarios can account for the stratigraphic variations in the $\delta^{13}C$ and $\delta^{44/40}Ca$ values of sedimentary carbonates across the Permian-Triassic transition, we used coupled box models of the geological carbon and calcium cycles following Bachan and Payne (2015) and Jost et al. (2017). As noted by Komar and Zeebe (2016), numerical models of both carbon and calcium must include a complete treatment of carbonate speciation and alkalinity. In this approach, seawater carbonate chemistry parameters, including alkalinity, saturation state (Ω), and pH, are calculated following the relationships described by Zeebe and Wolf-Gladrow (2001). Using a mass balance framework, variations in dissolved inorganic carbon (DIC) of seawater can be represented as:

$$\frac{dM_C}{dt} = F_{wcarb} + F_{worg} + F_{volc} - F_{borg} - F_{bcarb}, \quad (1)$$

and the associated carbon isotopic balance can be written as:

$$\begin{aligned}\frac{d\delta^{13}C}{dt} * M_C = {} & F_{wcarb}\left(\delta^{13}C_{wcarb} - \delta^{13}C_{sw}\right) + \\ & F_{worg}\left(\delta^{13}C_{worg} - \delta^{13}C_{sw}\right) + \\ & F_{volc}\left(\delta^{13}C_{volc} - \delta^{13}C_{sw}\right) - \\ & F_{borg}\left(\Delta_{borg}\right) - F_{bcarb}\left(\Delta_{bcarb}\right). \quad (2)\end{aligned}$$

Similarly, the mass balance of seawater calcium is represented as:

$$\frac{dM_{Ca}}{dt} = F_{wsil} + F_{wcarb} + F_{hyd} - F_{bcarb}, \quad (3)$$

with the associated isotopic balance described as:

$$\frac{d\delta^{44/40}Ca}{dt} * M_{Ca} =$$
$$F_{wsil}\left(\delta^{44/40}Ca_{wsil} - \delta^{44/40}Ca_{sw}\right) +$$
$$F_{wcarb}\left(\delta^{44/40}Ca_{carb} - \delta^{4/40}Ca_{sw}\right) +$$
$$F_{hyd}\left(\delta^{44/40}Ca_{hyd} - \delta^{44/40}Ca_{sw}\right) -$$
$$F_{bcarb}\Delta_{bcarb}. \quad (4)$$

The terms and initial values for Equations 1–4 are defined in Table DR2 (see footnote 1). A complete description of model equations was presented by Jost et al. (2017).

Using this framework, we explored four scenarios that would have unique consequences for the carbon and calcium isotopic composition of seawater and carbonate sediments (Fig. 8). At steady state, the calcium concentration of seawater in the model is 15 m*M*, i.e., greater than the present value of 10 mM based on constraints from fluid inclusions (Berner, 2004). The residence time of calcium in seawater at steady state in the model, calculated by dividing the reservoir size by the burial flux, is 570 k.y. This residence time is also somewhat longer than the equivalent calculation for the modern ocean (427 k.y.), based on a 10 m*M* concentration in seawater and a removal rate of 32 Tmol/yr (DePaolo, 2004). Due to uncertainties in residence times at steady state, as well as in other parameters, such as the strength of the silicate weathering feedback during Permian-Triassic time, the model runs are only intended to illustrate basic behaviors of the calcium cycle. Precisely reproducing the actual history of the Permian-Triassic calcium cycle is beyond the scope of possibility at present due to the uncertainties in both the model and the data.

The series of model experiments demonstrates a range of potential behaviors in the coupled carbon and calcium cycles that are expected to be recorded as isotope variations in sedimentary rocks. First, we ran a scenario meant to approximate the release of volcanic CO_2 from the Siberian Traps large igneous province, involving an input of 36,000 Pg (3×10^{18} mol) of carbon with a $\delta^{13}C$ composition of –15‰ over 200,000 k.y. Here, a negative excursion in $\delta^{13}C$ of 3‰ is associated with a negative excursion in $\delta^{44/40}Ca$ of <0.1‰ (Fig. 8A). This result supports previous arguments that a perturbation to the carbon and calcium cycles from volcanism alone is insufficient to explain the magnitude of the $\delta^{44/40}Ca$ excursion (Komar and Zeebe, 2016). This conclusion applies also to $\delta^{44/40}Ca$ records across the Paleocene-Eocene thermal maximum (Komar and Zeebe, 2011) and the end-Triassic extinction (Jost et al., 2017). Second, a global increase in the calcium fractionation factor (without a change in the dominant calcium carbonate polymorph), potentially caused by a change in precipitation rate (due to, for example, changing seawater carbonate saturation state) would produce no

meaningful change in $\delta^{13}C$ but a large excursion in $\delta^{44/40}Ca$ and is thus insufficient to account for the coincident excursions in $\delta^{13}C$ and $\delta^{44/40}Ca$. If the dominant carbonate polymorph at a studied stratigraphic section shifted from mixed calcite-aragonite sediments to all aragonite, the carbonate sediment $\delta^{44/40}Ca$ value would exhibit a negative excursion (Fig. 8B), because the fractionation factor for aragonite is ~0.6‰ larger than that for calcite (Gussone et al., 2005). Although the Permian-Triassic ocean is generally thought to have had a Mg/Ca ratio that generally favored aragonite precipitation (Stanley and Hardie, 1998), the ratio of aragonite to calcite precipitation is also controlled by temperature (Balthasar and Cusack, 2015) and, therefore, might have increased across the Permian-Triassic transition in association with a rise in global temperatures (Joachimski et al., 2012; Sun et al., 2012; Romano et al., 2013). The clear importance of factors other than the $\delta^{44/40}Ca$ value of seawater can further explain the earlier onset of the $\delta^{44/40}Ca$ excursion at Taşkent than at Dajiang through an earlier shift in original mineralogy or a change in local precipitation rate.

In comparison to changes in carbonate mineralogy, perturbations in marine carbonate chemistry can impact both seawater and carbonate $\delta^{44/40}Ca$ and $\delta^{13}C$ values. Specifically, carbonate chemistry can be altered if the earliest Triassic oceans were more anoxic (e.g., Wignall and Twitchett, 1996; Brennecka et al., 2011; Lau et al., 2016). Anaerobic respiratory pathways that cause alkalinity to increase, such as sulfate reduction, would become more important in a less oxygenated ocean. Carbonate burial rates would be expected to increase in response to an increase in alkalinity, because the increase in alkalinity would cause an increase in saturation state, all else being equal. The resulting imbalance between the calcium removal rate and the calcium delivery rate would cause $\delta^{44/40}Ca$ values in seawater and carbonate sediments to become more positive (Fig. 8C) while simultaneously causing $\delta^{13}C$ values to become more negative due to the increase in the proportional removal of carbon in the inorganic form. Additionally, anoxia can be a result of a more productive ocean: Following the volcanically triggered release of CO_2, enhanced silicate weathering would deliver more nutrients, such as phosphate, into the ocean and drive up productivity, oxygen demand, and organic carbon burial. In a scenario forced by an increase in phosphate delivery to the ocean, both $\delta^{13}C$ and $\delta^{44/40}Ca$ would exhibit positive excursions (Fig. 8D). The $\delta^{13}C$ value of carbonates increases because the enhanced phosphate delivery enables a greater proportion of carbon to be removed in the form of organic matter. The removal of organic matter causes a decrease in DIC but not alkalinity, driving up the carbonate burial flux as well. The resulting calcium flux imbalance causes a small increase in $\delta^{44/40}Ca$ (~0.1‰, close to instrument external reproducibility) of seawater and associated carbonate sediments.

A larger sensitivity analysis further confirmed the need for factors in addition to calcium flux imbalances to explain the magnitude of the observed $\delta^{44/40}Ca$ excursion in carbonate rocks. For this sensitivity analysis, we modeled the

responses of the carbon and calcium cycles to injections of volcanic carbon—between 5000 and 60,000 Pg carbon, with a carbon isotope composition between –5‰ and –60‰ (Fig. 9). In this model, we assumed a constant fractionation between carbonate sediments and seawater. We found that none of these model scenarios could account for the full magnitude of the observed $\delta^{44/40}$Ca excursion. At most, they accounted for approximately half of the observed magnitude (maximum possible was 0.13‰). Similar to previous results for a study of the end-Triassic mass extinction (Jost et al., 2017), our sensitivity analysis suggests that additional factors that affect the fractionation between seawater and carbonates are required to explain the full magnitude of the observed excursion through effects on the magnitude of fractionation locally. Such effects, which include original mineralogy and change in precipitation rate, can also account for apparent differences in the position of the onset of the negative excursion among sections (Fig. 6).

Given these model results, we suggest that the latest Changhsingian to earliest Griesbachian global parallel negative excursions in carbonate δ^{13}C and $\delta^{44/40}$Ca are best explained by a combination of volcanic outgassing, subsequent increased calcium input from silicate weathering, and either a temporary increase in the original proportion of aragonite in the sediment or an increase in the fractionation factor between carbonate sediments and seawater. This change in fractionation factor could be produced either by a shift toward a larger component of aragonite in the original sediment, because calcium isotopes are fractionated more during aragonite precipitation than during calcite precipitation (e.g., Gussone et al., 2005), or by an increase in the rate of carbonate precipitation, because calcium isotopes are fractionated more at higher precipitation rates (Tang et al., 2008). This scenario is consistent with the negative excursion observed in the $\delta^{44/40}$Ca values of biogenic apatite in conodont microfossils from the Meishan section, China (Hinojosa et al., 2012), although it suggests that the size of the calcium isotope excursion in biogenic apatite should be somewhat smaller than that in carbonate sediments.

The sedimentary rock record provides evidence consistent both with a shift in original mineralogy and with a potential increase in carbonate saturation state and mineral precipitation rate. Based on ooid growth experiments, for example, high carbonate saturation levels are required to account for the large sizes (up to 1 cm diameter) of Lower Triassic ooids (Trower et al., 2017). Although a rapid increase in volcanic CO_2outgassing may result in ocean acidification, compensation occurs such that the mean saturation level of seawater will be higher than background levels within 100 k.y. as the delivery of alkalinity from silicate weathering comes into equilibrium with the new, higher CO_2 input rate (Fig. 8A). Conceptually, if the input of CO_2 to the system increases, and if the removal rate is related to the carbonate saturation state of seawater, then the saturation state must eventually increase to balance the increased delivery rate. This is simply another way of viewing silicate weathering feedback, which is broadly viewed as the long-

term stabilizing feedback on Earth's climate (Walker et al., 1981). The smaller $\delta^{44/40}$Ca excursion displayed by the conodonts, which reflects the evolution of the seawater $\delta^{44/40}$Ca value, is independent from the fractionation factor between carbonate sediments and seawater and is consistent with increased calcium input from the continents via enhanced silicate weathering (Fig. 6). The increase in silicate weathering and calcium delivery to the oceans during the latest Changhsingian–earliest Griesbachian, which would be required to remove the excess carbon emitted at the time of the end-Permian extinction in order to return the system to steady state via the silicate weathering feedback, is further supported by the increase in the seawater $^{87}Sr/^{86}Sr$ values displayed globally (Korte et al., 2003, 2004; Song et al., 2015; Sedlacek et al., 2014).

Clarkson et al. (2015) suggested that low boron isotope ratios ($\delta^{11}B$) in lowermost Griesbachian dolomites from Oman reflect a rapid decrease in ocean pH coincident with base of the *I. isarcica* conodont zone. The $\delta^{44/40}$Ca data from multiple sections reported here and the results from our model do not support this hypothesized acidification event. It is possible that a transient ocean acidification event occurred during deposition of the base of the *I. isarcica* conodont zone, which also experienced an increase in ocean temperature (Sun et al., 2012; Romano et al., 2013), but better biostratigraphic resolution is still required to clearly demonstrate that these isotope anomalies were coeval across sections. The lack of data on the incorporation of boron isotopes into dolomites makes the assessment of the acidification event reported by Clarkson et al. (2015) rather difficult, and other mechanisms may explain the rapid decrease in $\delta^{11}B$ (Stewart et al., 2015). Laboratory experiments have shown an ~8‰ fractionation in the $\delta^{11}B$ value displayed by calcite and aragonite at pH 7 (Noireaux et al., 2015). Given the evidence enumerated herein for changes in carbonate polymorphs influencing the $\delta^{44/40}$Ca record, it is also possible that the negative shift in the $\delta^{11}B$ value of dolomites reported by Clarkson et al. (2015) could reflect a change from calcite to aragonite mineralogy as the locally dominant dolomite precursor polymorph at this horizon. The lack of constraints on the original mineralogy of the dolomite sections reported by Clarkson et al. (2015) may explain the lack of B isotope evidence of ocean acidification coinciding with the end-Permian mass extinction (Payne et al., 2010).

CONCLUSIONS

A negative $\delta^{44/40}$Ca anomaly occurs in several globally distributed Changhsingian–Griesbachian carbonate successions. These data confirm that the PTB $\delta^{44/40}$Ca excursion initially identified in China was global in extent. Forward modeling incorporating coupling between the global carbon and calcium cycles indicates that the calcium isotope anomaly is best interpreted to have resulted from a combination of imbalances in the geological calcium cycle driven by ocean acidification and subsequent enhanced silicate weathering, as well as changes in the dominant carbonate mineralogy and, perhaps, the marine carbonate saturation state, which increased the

fractionation of calcium isotopes as carbonate sediment production increased. Such a scenario is consistent not only with emerging calcium isotope constraints on geological calcium cycle dynamics, but also with carbon isotope evidence for a large carbon release event, oxygen isotope evidence for dramatic global warming, and paleontological evidence for the preferential extinction of marine animals most susceptible to the effects of acidification, warming, and anoxia.

ACKNOWLEDGMENTS

Juan Carlos Silva-Tamayo is thankful to the European Commission for its support for the Permian-Triassic CaS project throughout the Marie Curie International Fellowship Program. Silva-Tamayo is also thankful to the University of Houston for providing funding throughout the assistant professor start-up seed funding, and to Colciencias for providing funding through grant 727771451027, “Quantifying the effects of ocean acidification and de-oxygenation on the marine biogeochemical cycles during periods of high atmospheric pCO_2: Implications for the future of the 21st century oceans.” The project was supported by grants to Jonathan L. Payne and Adina Paytan (U.S. National Science Foundation grant EAR-0807377 to Payne and National Aeronautics and Space Administration grant NNX09AN67G to Payne and Paytan). Shaun Brown, Donald J. Depaolo, and the Berkeley Center for Isotope Geochemistry are supported by the U.S. Department of Energy, Office of Science, Office of Basic Energy Sciences, Chemical Sciences, Geosciences, and Biosciences Division, under award number DE-AC02–05CH11231. Silva-Tamayo, Robert J. Newton, and Sylvain Richoz conducted field work in Oman under authorization of the Public Authority for Mining, Sultanate of Oman. Richoz was sponsored for field work by the Austrian National Committee for IGCP (IGCP630) and thanks A. Baud for earlier field work.

References

Bachan, A., and Payne, J.L., 2016, Modelling the impact of pulsed CAMP volcanism on pCO2 and δ13C across the Triassic–Jurassic transition: Geological Magazine, v. 153, p. 252–270, https://doi.org/10.1017/S0016756815000126.

Balthasar, U., and Cusack, M., 2015, Aragonite-calcite seas: Quantifying the gray area: Geology, v. 43, p. 99–102, https://doi.org/10.1130/G36293.1.

Baud, A., and Richoz, S., 2013, Permian-Triassic transition and the Saiq/Mahil boundary in the Oman Mountains: Proposed correction for lithostratigraphic nomenclature: Geoarabica, v. 18, p. 87–98.

Berner, R.A., 2002, Examination of hypotheses for the Permo-Triassic boundary extinction by carbon cycle modeling: Proceedings of the National Academy of the United States of America, v. 99, p. 4172–4177, https://doi.org/10.1073/pnas.032095199.

Berner, R.A., 2004, A model for calcium, magnesium and sulfate in seawater over Phanerozoic time: American Journal of Science, v. 304, p. 438–453, https://doi.org /10.2475/ajs.304.5.438.

Blättler, C.L., Henderson, G.M., and Jenkyns, H.C., 2012, Explaining the Phanerozoic Ca isotope history of seawater: Geology, v. 40, p. 843–846, https://doi.org/10 .1130/G33191.1.

Böhm, F., Gussone, N., Eisenhauer, A., Dullo, W-Chr., Reynaud, S., and Paytan, A., 2006, Calcium isotope fractionation in modern scleractinian corals: Geochimica et Cosmochimica Acta, v. 70, p. 4452–4462, https://doi.org/10.1016/j.gca.2006.06.1546.

Brandner, R., Horacek, M., and Keim, L., 2012, PermianTriassic boundary and Lower Triassic in the Dolomites, southern Alps (Italy): Journal of Alpine Geology, v. 54, p. 379–404.

Brennecka, G.A., Herrmann, A.D., Algeo, T.J., and Anbar, A.D., 2011, Rapid expansion of oceanic anoxia immediately before the end-Permian mass extinction: Proceedings of the National Academy of Sciences of the United States of America, v. 108, p. 17,631–17,634, https://doi.org/10.1073/pnas.1106039108.

Burgess, S., Bowring, S., and Shen, S., 2014, High-precision timeline for Earth's most severe extinction: Proceedings of the National Academy of Sciences of the United States of America, v. 109, p. 1–6.

Chen, J., Beatty, T.W., Henderson, C.M., and Rowe, H., 2009, Conodont biostratigraphy across the PermianTriassic boundary at the Dawen section, Great Bank of Guizhou, Guizhou Province, South China: Implications for the Late Permian extinction and correlation with Meishan: Journal of Asian Earth Sciences, v. 36, p. 442–458, https://doi.org/10.1016/j.jseaes.2008.08 .002.

Clarkson, M., Richoz, S., Wood, R., Maurer, F., Krystyn, L., McGurty, D.J., and Astratti, D., 2013, A new highresolution δ13C record for the Early Triassic: Insights from the Arabian Platform: Gondwana Research, v. 24, p. 233–242, https://doi.org/10.1016/j.gr.2012.10.002.

Clarkson, M., Kasemann, S.A., Wood, R.A., Lenton, T.M., Daines, S.J., Richoz, S., Ohnemueller, F., Meixner, A., Poulton, S.W., and Tipper, E.T., 2015, Ocean acidification and the Permo-Triassic mass extinction: Science, v. 348, p. 229–232, https://doi.org/10.1126/science .aaa0193.

Crasquin-Soleau, S., Richoz, S., Marcoux, J., Angiolini, L., Nicora, A., and Baud, A., 2002, The events of the Permian-Trias boundary: Last survivors and/or first colonisers among the ostracods of the Thurides (southwestern Turkey): Comptes Rendus Geoscience, v. 334, p. 489–495, https://doi.org/10.1016/S1631-0713 (02)01782-0.

DePaolo, D.J., 2004, Calcium isotopic variations produced by biological, kinetic, radiogenic and nucleosynthetic processes: Reviews in Mineralogy

and Geochemistry, v. 55, p. 255–288, https://doi.org/10.2138/gsrmg.55.1.255.

DePaolo, D.J., 2011, Surface kinetic model for isotopic and trace element fractionation during precipitation of calcite from aqueous solutions: Geochimica et Cosmochimica Acta, v. 75, p. 1039–1056, https://doi.org/10 .1016/j.gca.2010.11.020.

Erwin, D.H., 1994, The Permo-Triassic extinction: Nature, v. 367, p. 231–236, https://doi.org/10.1038/367231a0.

Erwin, D.H., Bowring, S.A., and Yugan, J., 2002, EndPermian mass extinctions: A review, in Koeberl, C., and MacLeod, K.G., eds., Catastrophic Events and Mass Extinctions: Impacts and Beyond: Boulder, Colorado, Geological Society of America Special Paper 356, p. 363–383, https://doi.org/ 10.1130/0-8137-2356-6.363.

Fantle, M.S., 2010, Evaluating the Ca isotope proxy: American Journal of Science, v. 310, p. 194–230, https://doi .org/10.2475/03.2010.03.

Fantle, M.S., and DePaolo, D.J., 2007, Ca isotopes in carbonate sediment and pore fluid from ODP Site 807A: The Ca2(aq)-calcite equilibrium fractionation factor and calcite recrystallization rates in Pleistocene sediments: Geochimica et Cosmochimica Acta, v. 71, p. 2524–2546, https://doi.org/10.1016/j.gca.2007.03 .006.

Fantle, M.S., and Higgins, J., 2014, The effects of diagenesis and dolomitization on Ca and Mg isotopes in marine platform carbonates: Implications for the geochemical cycles of Ca and Mg: Geochimica et Cosmochimica Acta, v. 142, p. 458–481, https://doi.org/10.1016/j.gca .2014.07.025.

Fantle, M.S., and Tipper, E., 2014, Calcium isotopes in the global biogeochemical Ca cycle: Implications for development of a Ca isotope proxy: Earth-Science Reviews, v. 129, p. 148–177, https://doi.org/10.1016/j .earscirev.2013.10.004.

Farabegoli, E., and Perri, M.C., 1998, Permian/Triassic boundary and Early Triassic of the Bulla section (southern Alps, Italy): Lithostratigraphy, facies and conodont biostratigraphy: Giornale di Geologia, ser. 3a (special issue, ECOS VII Southern Alps Fieldtrip Guidebook), v. 60, p. 292–311.

Farkaš, J., Böhm, F., Wallmann, K., Blenkinsop, J., Eisenhauer, A., van Geldern, R., Munnecke, A., Voigt, S., and Veizer, J., 2007a, Calcium isotope record of Phanerozoic oceans: Implications for chemical evolution of seawater and its causative mechanisms: Geochimica et Cosmochimica Acta, v. 71, p. 5117–5134, https://doi .org/10.1016/j.gca.2007.09.004.

Farkaš, J., Buhl, D., Blenkinsop, J., and Veizer, J., 2007b, Evolution of the oceanic calcium cycle during the late Mesozoic: Evidence from 44/40 Ca of marine skeletal carbonates: Earth and Planetary Science Letters, v. 253, p. 96–111, https://doi.org/10.1016/j.epsl.2006 .10.015.

Groves, J.R., and Altiner, D., 2005, Survival and recovery of calcareous foraminifera pursuant to the end-Permian mass extinction: Comptes Rendus Palévol, v. 4, p. 487– 500, https://doi.org/10.1016/j.crpv.2004.12.007.

Groves, J.R., Altiner, D., and Rettori, R., 2005, Extinction, survival, and recovery of lagenide foraminifers in the Permian-Triassic boundary interval, central Taurides, Turkey: Journal of Paleontology, v. 79, p. 1–38, https://doi.org/10.1666/0022-3360(2005)79[1:ESAROL]2.0 .CO;2.

Gussone, N., Böhm, F., Eisenhauer, A., Dietzel, M., Heuser, A., Teichert, B.M.A., Reitner, J., Worheide, G., and Dullo, W.C., 2005, Calcium isotope fractionation in calcite and aragonite: Geochimica et Cosmochimica Acta, v. 69, p. 4485–4494, https://doi.org/10.1016/j .gca.2005.06.003.

Heuser, A., Eisenhauer, A., Gussone, N., Bock, B., Hansen, B.T., and Nägler, T.F., 2002, Measurements of calcium isotopes (δ44Ca) using a TIMS multicollector technique: International Journal of Mass Spectrometry, v. 220, p. 385–397, https://doi.org/10.1016/S1387 -3806(02)00838-2.

Heuser, A., Eisenhauer, A., Böhm, F., Wallmann, K., Gussone, N., Pearson, P., Nägler, T.F., and Dullo, W.C., 2005, Calcium isotope (δ44/40Ca) variations of Neogene planktonic foraminifera: Paleoceanography, v. 20, PA2013, https://doi.org/10.1029/2004PA001048.

Hinojosa, J.L., Brown, S.T., DePaolo, D.J., Paytan, A., Shen, S., Chen, J., and Payne, J.L., 2012, Evidence for endPermian ocean acidification from calcium isotopes in biogenic apatite: Geology, v. 40, p. 743–746, https://doi.org/10.1130/G33048.1.

Hippler, D., Schmitt, A.D., Gussone, N., Heuser, A., Stille, P., Eisenhauer, A. and Nägler, T.F., 2003, Ca isotopic composition of various standards and seawater: Geostandards Newsletters, v. 27, p. 13–19.

Holmden, C., Papanastassiou, D.A., Blanchon, P., and Evans, S., 2012, δ44/40Ca variability in shallow water carbonates and the impact of submarine groundwater discharge on Ca-cycling in marine environments: Geochimica et Cosmochimica Acta, v. 83, p. 179–194, https://doi.org/10.1016/j.gca.2011.12.031.

Jacobson, A.D., and Holmden, C., 2008, δ44Ca evolution in a carbonate aquifer and its bearing on the equilibrium isotope fractionation factor for calcite: Earth and Plan-etary Science Letters, v. 270, p. 349–353, https://doi .org/10.1016/j.epsl.2008.03.039.

Jiang, H.-S., Lai, X.-L., Sun, Y.-D., Wignall, P.B., Liu, J.-B., and Yan, C.-B., 2014, Permian-Triassic conodonts from Dajiang (Guizhou, South China) and their implication for the age of microbialite deposition in the aftermath of the end-Permian mass extinction: Journal of Earth Science, v. 25, p. 413–430, https://doi.org/10 .1007/S12583-014-0444-4.

Joachimski, M.M., Lai, X., Shen, S., Jiang, H., Luo, G., Chen, B., Chen, J., and Sun, Y., 2012, Climate warming in the latest Permian and the Permian-

Triassic mass extinction: Geology, v. 40, p. 195–198, https://doi.org/10.1130/G32707.1.

Jost, A.B., Bachan, A., van de Schootbrugge, B., Brown, S.T., DePaolo, D.J., and Payne, J.L., 2017, Additive effects of acidification and mineralogy on calcium isotopes in Triassic/Jurassic boundary limestones: Geochemistry Geophysics Geosystems, v. 18, p. 113–124, https://doi.org/10.1002/2016GC006724.

Kelley, B.M., Yu, M., Lehrmann, D.J., Jost, A.B., Meyer, K.M., and Payne, J.L., 2011, An updated model of the stratigraphic architecture of the Great Bank of Guizhou, an isolated carbonate platform in the Nanpanjiang Basin of South China: American Association of Petroleum Geologists Search and Discovery article 90124.

Koehrer, B., Zeller, M., Aigner, T., Pöppelreiter, M., Milroy, P., Forke, H., and Al-Kindi, S., 2010, Facies and stratigraphic framework of a Khuff outcrop equivalent: Saiq and Mahil formations, Al Jabal al-Akhdar, Sultanate of Oman: GeoArabia, v. 15, no. 2, p. 91–156.

Komar, N., and R.E. Zeebe, 2011, Oceanic calcium changes from enhanced weathering during the PaleoceneEocene thermal maximum: No effect on calcium-based proxies: Paleoceanography, v. 26, PA3211, https://doi.org/10.1029/2010PA001979.

Komar, N., and Zeebe, R.E., 2016, Calcium and calcium isotope changes during carbon cycle perturbations at the end-Permian: Paleoceanography, v. 31, p. 115–130, https://doi.org/10.1002/2015PA002834.

Korte, C., and Kozur, H., 2010, Carbon-isotope stratigraphy across the Permian-Triassic boundary: A review: Journal of Asian Earth Sciences, v. 39, p. 215–235, https:// doi.org/10.1016/j.jseaes.2010.01.005.

Korte, C., Kozur, H.W., Bruckschen, P., and Veizer, J., 2003, Strontium isotope evolution of Late Permian and Triassic seawater: Geochimica et Cosmochimica Acta, v. 67, p. 47–62, https://doi.org/10.1016/S0016-7037(02)01035-9.

Korte, C., Kozur, H.W., Joachimski, M.M., Strauss, H., Veizer, J., and Schwark, L., 2004, Carbon, sulfur, oxygen, and strontium isotope records, organic geochemistry and biostratigraphy across the Permian/Triassic boundary in Abadeh, Iran: International Journal of Earth Sciences, v. 93, p. 565–581.

Lau, K.V., Maher, K., Altiner, D., Kelley, B.M., Kump, L.R., Lehrmann, D.J., Silva-Tamayo, J.C., Weaver, K.L., Yu, M., and Payne, J.L., 2016, Marine anoxia and delayed Earth system recovery after the end-Permian extinction: Proceedings of the National Academy of Sciences of the United States of America, v. 113, no. 9, p. 2360– 2365, https://doi.org/10.1073/pnas.1515080113.

Lau, K.V., Maher, K., Brown, S.T., Jost, A.B., Altiner, D., DePaolo, D.J., Eisenhauer, A., Kelley, B.M., Lehrmann, D.J., Paytan, A., Yu, M., Silva-Tamayo,

J.C., and Payne, J.L., 2017, The influence of seawater carbonate chemistry, mineralogy, and diagenesis on calcium isotope variations in Lower-Middle Triassic carbonate rocks: Chemical Geology, v. 4271, p. 13–37, https://doi .org/10.1016/j.chemgeo.2017.09.006.

Lehrmann, D.J., Jiayong, W., and Enos, P., 1998, Controls on facies architecture of a large Triassic carbonate platform: The Great Bank of Guizhou, Nanpanjiang Basin, South China: Journal of Sedimentary Research, v. 68, p. 311–326, https://doi.org/10.2110/jsr.68.311.

Lehrmann, D.J., Ramezani, J., Bowring, S.A., Martin, M.W., Montgomery, P., Enos, P., Payne, J.L., Orchard, M.J., Wang, H., and Wei, J., 2006, Timing of recovery from the end-Permian extinction: Geochronologic and biostratigraphic constraints from South China: Geology, v. 34, p. 1053–1056, https://doi.org/10.1130 /G22827A.1.

Lehrmann, D.J., Minzoni, M., Li, X., Yu, M., Payne, J.L., Kelley, B.M., Schaal, E.K., and Enos, P., 2012, Lower Triassic oolites of the Nanpanjiang Basin, South China: American Association of Petroleum Geologists Bulletin, v. 96, p. 1389–1414, https://doi.org/10.1306 /01231211148.

Newton, R.J., Pevitt, E.L., Wignall, P.B., and Bottrell, S.H., 2004, Large shifts in the isotopic composition of seawater sulphate across the Permo-Triassic boundary in northern Italy: Earth and Planetary Science Letters, v. 218, p. 331–345, https://doi.org/10.1016/S0012 -821X(03)00676-9.

Nielsen, L.C., Druhan, J.L., Yang, W., Brown, S.T., and DePaolo, D.J., 2012, Calcium isotopes as tracers of biogeochemical processes, in Baskaran, M., ed., Handbook of Environmental Isotope Geochemistry: Springer, p. 105–124.

Noireaux, J., Mavromatis, V., Gaillardet, J., Schott, J., Montouillout, V., Louvat, P., Rollion-Bard, C., and Neuville, D.R., 2015, Crystallographic control on the boron isotope paleo-pH proxy: Earth and Planetary Science Letters, v. 430, p. 398–407, https://doi.org/10 .1016/j.epsl.2015.07.063.

Payne, J.L., and Clapham, M.E., 2012, End-Permian mass extinction in the oceans: An ancient analog for the 21st century?: Annual Review of Earth and Planetary Sciences, v. 40, p. 89–111, https://doi.org/10.1146 /annurev-earth-042711-105329.

Payne, J.L., Lehrmann, D.J., Christensen, S., Wei, J., and Knoll, A.H., 2006a, Environmental and biological controls on the initiation and growth of a Middle Triassic (Anisian) reef complex on the Great Bank of Guizhou, Guizhou Province, China: Palaios, v. 21, p. 325–343, https://doi.org/10.2110/palo.2005.P05-58e.

Payne, J.L., Lehrmann, D.J., Wei, J., and Knoll, A.H., 2006b, The pattern and timing of biotic recovery on the Great Bank of Guizhou, Guizhou Province, China: Palaios, v. 21, p. 63–85, https://doi.org/10.2110/palo .2005.p05-12p.

Payne, J.L., Lehrmann, D.J., Follett, D., Seibel, M., Kump, L.R., Riccardi, A., Altiner, D., Sano, H., and Wei, J., 2007, Erosional truncation of uppermost

Permian carbonates and implications for Permian-Triassic boundary events: Geological Society of America Bulletin, v. 119, p. 771–784, https://doi.org/10.1130/B26091.1.

Payne, J.L., Turchyn, A.V., Paytan, A., DePaolo, D.P., Lehrmann, D.J., Yu, Y., and Wei, J., 2010, Calcium isotope constraints on the end-Permian mass extinction: Proceedings of the National Academy of the United States of America, v. 107, p. 8543–8548, https://doi.org/10 .1073/pnas.0914065107.

Perez-Gomez, I., Farquani, S., Claps, M., and Peter, H., 2014, Diagenetic evolution of a Permo-Triassic Khuff oolitic reservoir in north Oman, in Pöppelreiter, M., ed., Permo-Triassic Sequence of the Arabian Plate: European Association of Geoscientists and Engineers, p. 327–386.

Perri, C.M., 1991, Conodont biostratigraphy of the Werfen Formation (Lower Triassic), southern Alps, Italy: Bollettino della Società Paleontologica Italiana, v. 30, p. 23–45.

Perri, C.M., and Farabegoli, E., 2003, Conodonts across the Permian-Triassic boundary in the Southern Alps: Courier Forschungsinstitute Senckenberg, v. 245, p. 281–313.

Pruss, S.B., Bottjer, D.J., Corsetti, F.A., and Baud, A., 2006, A global marine sedimentary response to the endPermian mass extinction: Examples from southern Turkey and the western United States: Earth-Science Reviews, v. 78, p. 193–206, https://doi.org/10.1016/j .earscirev.2006.05.002.

Richoz, S., 2004, Stratigraphie et Variations Isotopiques du Carbone dans le Permien Supérieur et le Trias Inférieur de la Néotéthys (Turquie, Oman et Iran) [Ph.D. thesis]: Lausanne, Switzerland, Lausanne University, 303 p.

Richoz, S., Krystyn, L., Baud, A., Brandner, R., Horacek, M., and Mohtat-Aghai, P., 2010a, Permian-Triassic boundary interval in the Middle East (Iran and N. Oman): Progressive environmental change from detailed carbonate carbon isotope marine curve and sedimentary evolution: Journal of Asian Earth Sciences, v. 39, p. 236–253, https://doi.org/10.1016/j.jseaes.2009.12.014.

Richoz, S., Krystyn, L., Weidlich, O., Baud, A., Beauchamp, B., Bernecker, M., Cordey, F., Grasby, S., Henderson, C., Marcoux, J., Nicora, A., and Twitchett, R., 2010b, The Permian-Triassic transition in the Oman Mountains: Transect of the Tethyan margin from shallow to deepwater deposits, in Baud, A., and Bernecker, M., eds., IGCP 572 Field Guide Book 2: Muscat, Oman, Gutech Geoscience Workshop Publication 1, 109 p.

Richoz, S., Baud, A., Beauchamp, B., Grasby, S., Henderson, C., and Krystyn, L., 2014, Khuff margin: Slope to oceanic deposits (Permian-Triassic Allochthons and Exotics, Oman), in Pöppelreiter, M., ed., The Khuff Formation: New Perspective: Houten, Netherlands, EAGE Publications, p. 55–76.

Romano, C., Goudemand, N., Vennemann, T., Ware, D., Schneebeli-Hermann, E., Hochuli, P.A., Brühwiler, T., Brinkmann, W., and Bucher, H., 2013, Climatic and biotic upheavals following the end-Permian mass extinction: Nature Geoscience, v. 6, p. 57–60, https://doi .org/10.1038/ngeo1667.

Sedlacek, A.R., Saltzman, M.R., Algeo, T.J., Horacek, M., Brandner, R., Foland, K., and Denniston, R.F., 2014, 87Sr/86Sr stratigraphy from the Early Triassic of Zal, Iran: Linking temperature to weathering rates and the tempo of ecosystem recovery: Geology, v. 42, p. 779– 782, https://doi.org/10.1130/G35545.1.

Shen, S.Z., Crowley, J.L., Wang, Y., Bowring, S.A., Erwin, D.H., Sadler, P.M., Cao, C., Rothman, D.H., Henderson, C.M., Ramezani, J., Zhang, H., Shen, Y., Wang, X., Wang, W., Mu, L., Li, W., Tang, Y., Liu, X., Liu, L., Zeng, Y., Jiang, Y., and Jin, Y., 2011, Calibrating the end-Permian mass extinction: Science, v. 334, p. 1367– 1372, https://doi.org/10.1126/science.1213454.

Silva-Tamayo, J.C., Nägler, T.F., Nogueira, A., Kyser, K., Villa Igor, Riccomini, C., Sial., A.N., Narbonne, G.M., and James, N.P., 2010a, Global perturbation of the marine Ca-isotopic composition in the aftermath of the Marinoan global glaciation: Precambrian Research, v. 182, p. 373–381.

Silva-Tamayo, J.C., Nägler, T.F., Villa, I.M., Kyser, K., Vieira, L.C., Sial, A.N., Narbonne, G.M., and James, N.P., 2010b, Global Ca isotope variations in post-Sturtian carbonate successions: Terra Nova, v. 22, p. 188–194, https://doi.org/10.1111/j.1365-3121.2010.00933.x.

Song, H., Wignall, P.B., Tong, J., and Yin, H., 2012, Two pulses of extinction during the Permian-Triassic crisis: Nature Geoscience, v. 6, p. 52–56.

Song, H., Wignall, P.B., Tong, J., Song, H., Chen, J., Chu, D., Tian, L., Luo, M., Zong, K., Chen, Y., Lai, X., Zhang, K., and Wang, H., 2015, Integrated Sr isotope variations and global environmental changes through the Late Permian to early Late Triassic: Earth and Planetary Science Letters, v. 424, p. 140–147, https://doi .org/10.1016/j.epsl.2015.05.035.

Stanley, M.S., and Hardie, L.A., 1998, Secular oscillations in the carbonate mineralogy of reef-building and sediment-producing organisms driven by tectonically forced shifts in seawater chemistry: Palaeogeography, Palaeoclimatology, Palaeoecology, v. 144, p. 3–19, https://doi.org/10.1016/S0031-0182(98)00109-6.

Stewart, J.A., Gutjahr, M., Pearce, F., Swart, P.K., and Foster, G.L., 2015, Boron during meteoric diagenesis and its potential implications for Marinoan snowball Earth δ11B-pH excursions: Geology, v. 43, p. 627–630, https://doi.org/10.1130/G36652.1.

Sun, Y., Joachimski, M.M., Wignall, P.B., Yan, C., Chen, Y., Jiang, H., Wang, L., and Lai, X., 2012, Lethally hot temperatures during the Early Triassic greenhouse: Science, v. 338, p. 366–370, https://doi.org/10.1126 /science.1224126.

Tang, J., Kohler, S.J., and Dietzel, M., 2008, Sr2+/Ca2+ and 44Ca/40Ca fractionation during inorganic calcite formation: II. Ca isotopes: Geochimica et Cosmochimica Acta, v. 72, p. 3733–3745, https://doi.org/10.1016/j .gca.2008.05.033.

Tian, L., Bottjer, D.J., Tong, J., Li, F., Yang, T., Song, H., Song, H., and Liang, L., 2015, Distribution and size variation of ooids in the aftermath of the PermianTriassic mass extinction: Palaios, v. 30, p. 714–727, https://doi.org/10.2110/palo.2014.110.

Trower, E.J., Lamb, M.J., and Fischer, W.W., 2017, Experimental evidence that ooid size reflects a dynamic equi-librium between rapid precipitation and abrasion rates: Earth and Planetary Science Letters, v. 468, p. 112– 118, https://doi.org/10.1016/j.epsl.2017.04.004.

Ünal, E., Altiner, D., Yilmaz, I.O., and Ozkan-Altiner, S., 2003, Cyclic sedimentation across the Permian-Triassic boundary (Central Taurides, Turkey): Rivista Italiana di Paleontologia e Stratigrafia, v. 109, no. 2, p. 359–376.

Vasconcelos, C., McKenzie, J.A., Warthmann, R., and Bernasconi, S., 2005, Calibration of the δ18O paleothermometer with dolomite formed in microbial cultures and natural environments: Geology, v. 33, p. 317–320, https://doi.org/10.1130/G20992.1.

Walker, J.C.G., Hays, P.B., and Kasting, J.F., 1981, A negative feedback mechanism for the long-term stabilization of Earth’s surface temperature: Journal of Geophysical Research, v. 86, p. 9776–9782, https://doi .org/10.1029/JC086iC10p09776.

Watkins, J.M., DePaolo, D.J., and Watson, E.B., 2017, Kinetic fractionation of non-traditional stable isotopes by diffusion and crystal growth reactions: Reviews in Mineralogy and Geochemistry, v. 82, p. 85–125, https://doi.org/10.2138/rmg.2017.82.4.

Wignall, P.B., and Hallam, A., 1992, Anoxia as a cause of the Permian/Triassic extinction: Facies evidence from northern Italy and the western United States: Palaeogeography, Palaeoclimatology, Palaeoecology, v. 93, p. 21–46, https://doi.org/10.1016/0031-0182 (92)90182-5.

Wignall, P.B., and Twitchett, R.J., 1996, Ocean anoxia and the end-Permian mass extinction: Science, v. 272, p. 1155–1158, https://doi.org/10.1126/science.272 .5265.1155.

Zeebe, R.E., and Wolf-Gladrow, D.A., 2001, CO2 in Seawater: Equilibrium, Kinetics, Isotopes: Amsterdam, Netherlands, Elsevier, Oceanography Series 65, 346 p., https://doi.org/10.1016/S0924-7963(02)00179-3.

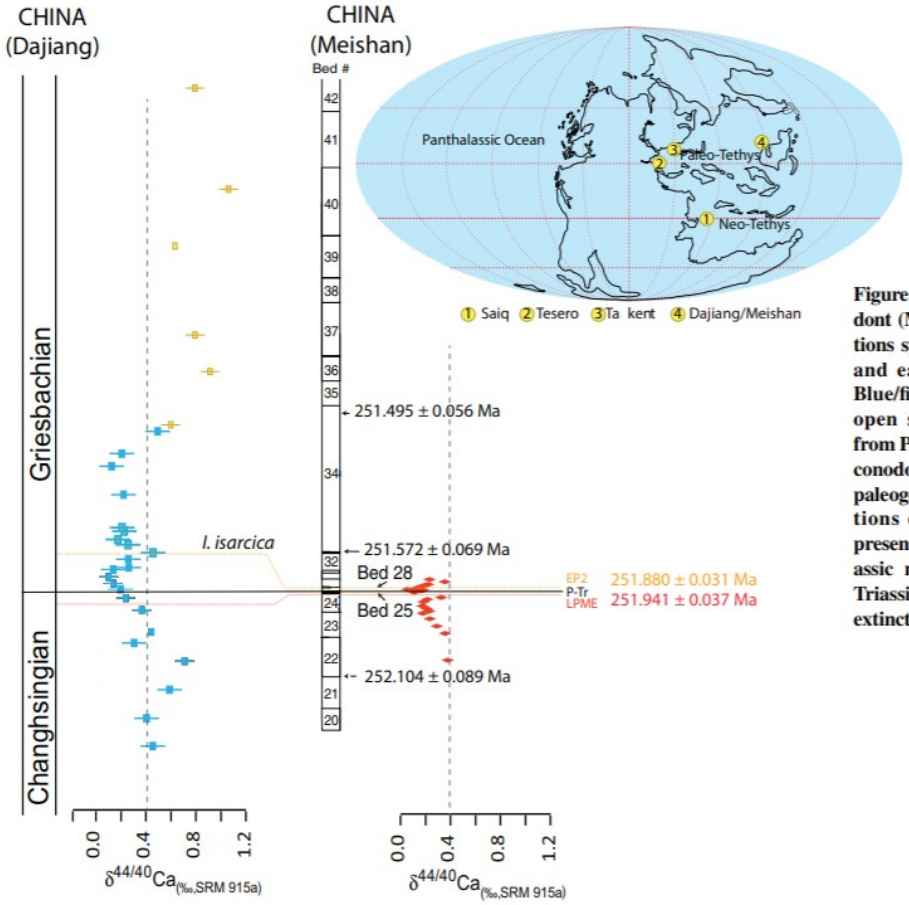

Figure 1. Carbonate (Dajiang) and conodont (Meishan) calcium isotope compositions spanning the latest Changhsingian and earliest Griesbachian in China. Blue/filled squares—limestone; yellow/open squares—dolomite (carbonates from Payne et al., 2010); red diamonds—conodonts (Hinojosa et al., 2012). The paleogeographic map presents the locations of these successions and those presented in this study. EP2—Early Triassic mass extinction; P-Tr—Permian-Triassic; LPME—Late Permian mass extinction; *I.*—*Isarcicella*.

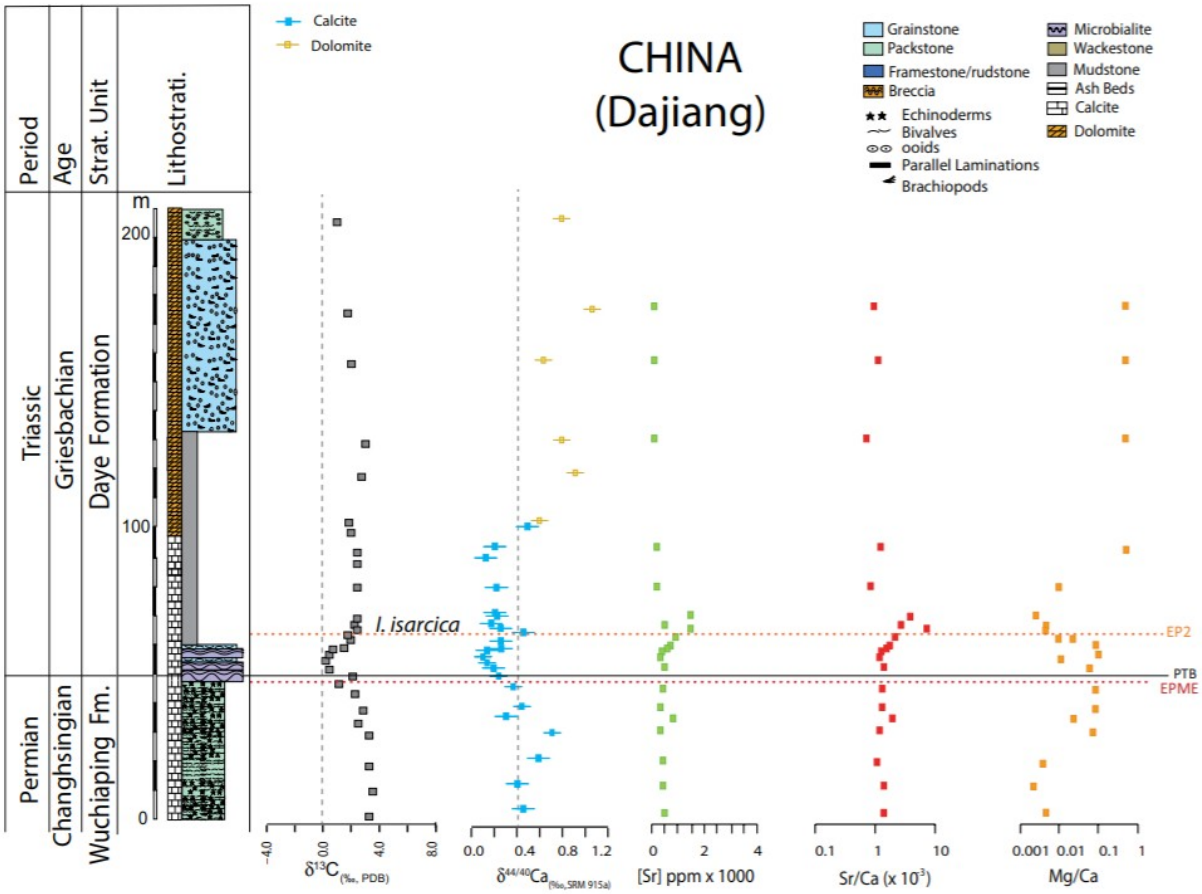

Figure 2. Lithostratigraphy and chemostratigraphy of the Dajiang section, Great Bank of Guizhou, South China. EPME—end-Permian mass extinction; PTB—Permian-Triassic boundary; EP2—Early Triassic mass extinction; PDB—Peedee belemnite; *I.*—*Isarcicella*. Data were previously published in Payne et al. (2010) and Lau et al. (2017).

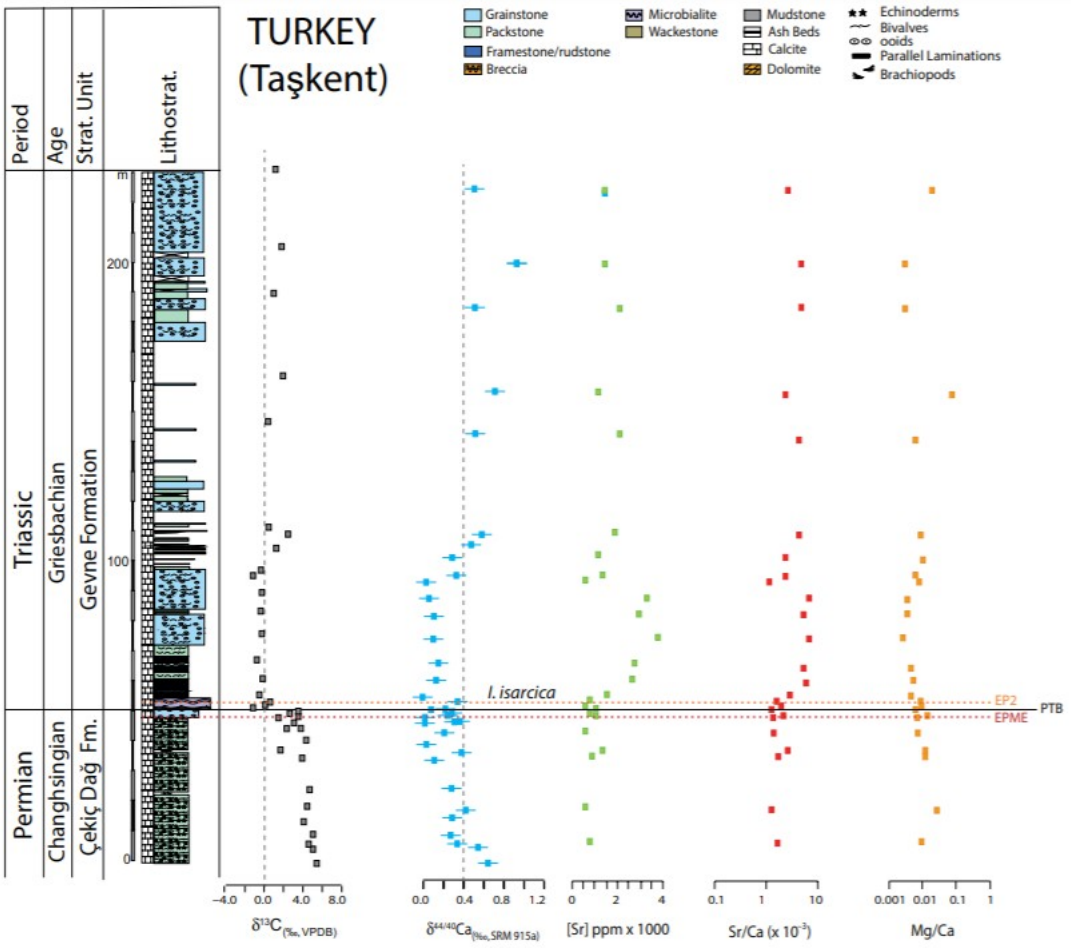

Figure 3. Lithostratigraphy and chemostratigraphy of the Çekiç Dağ and Gevne Formations, Taşkent section, Taurus Mountains, southern Turkey. EPME—end-Permian mass extinction; PTB—Permian-Triassic boundary; EP2—Early Triassic mass extinction; PDB—Peedee belemnite; *I.*—*Isarcicella*. Data were previously published in Lau et al. (2017).

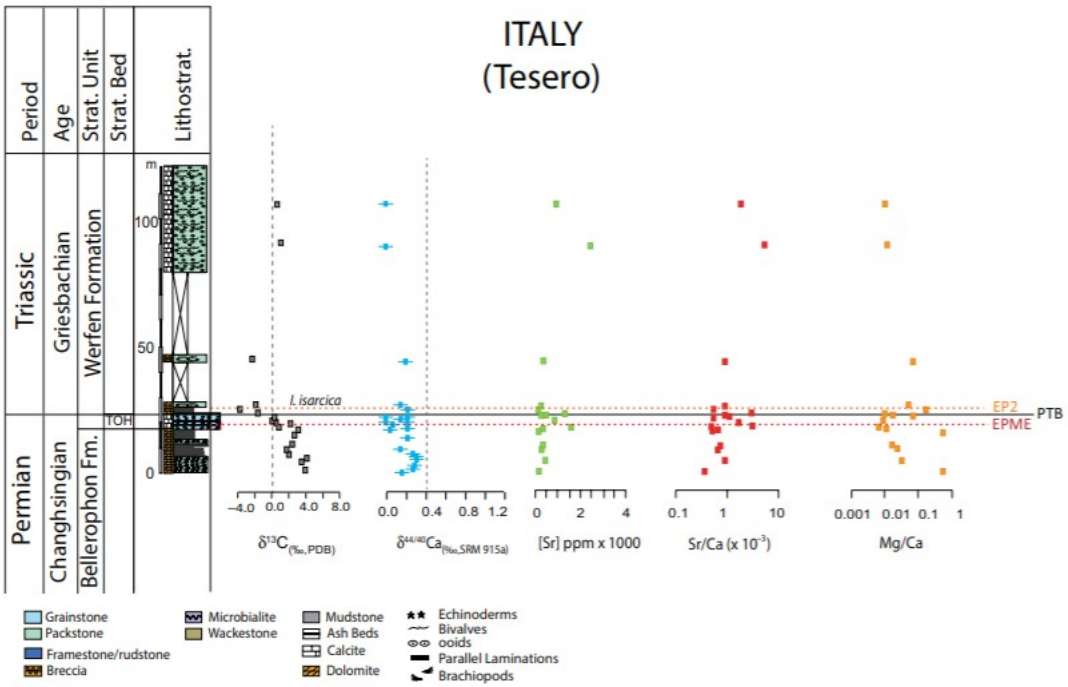

Figure 4. Lithostratigraphy and chemostratigraphy of the Bellerophon and Werfen Formations, Tesero Road section, Italian Dolomite Mountains, NE Italy. EPME—end-Permian mass extinction; PTB—Permian-Triassic boundary; EP2—Early Triassic mass extinction; PDB—Peedee belemnite; *I.—Isarcicella*.

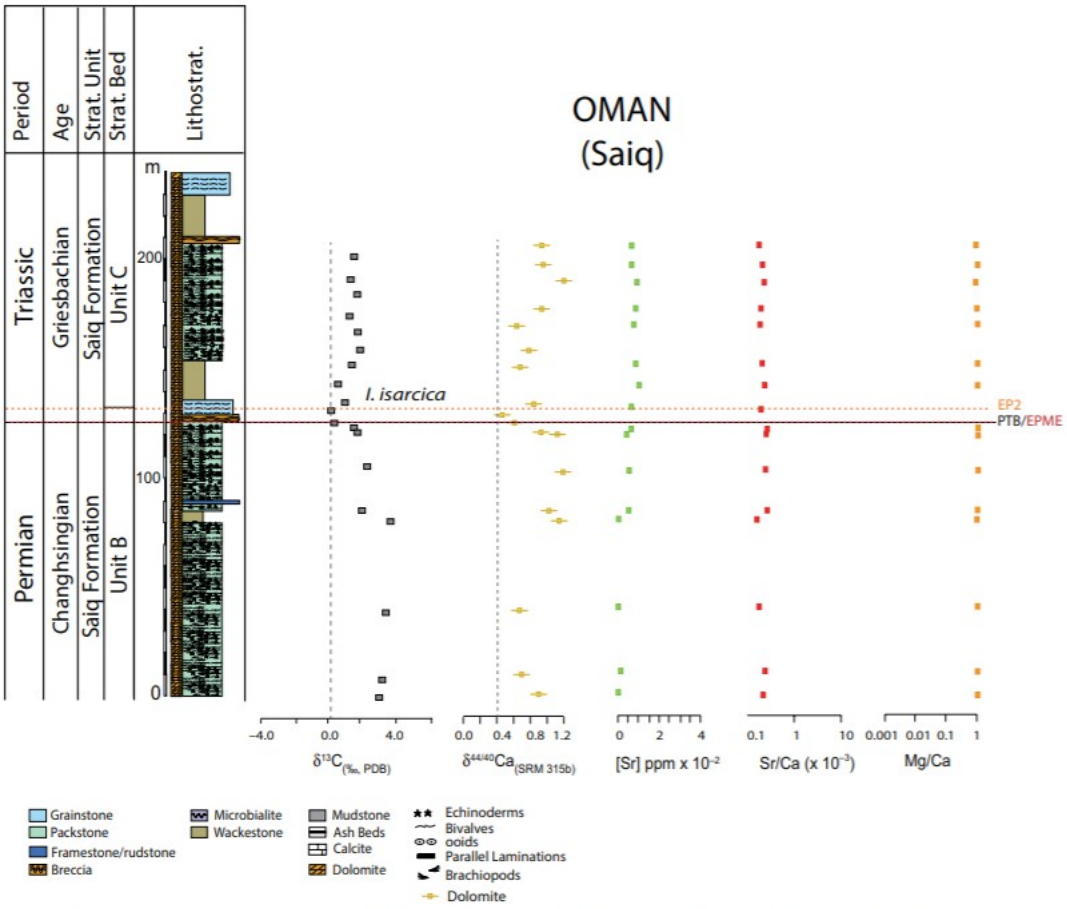

Figure 5. Lithostratigraphy and chemostratigraphy of the Saiq Formation, Saiq Plateau, Sultanate of Oman. EPME—end-Permian mass extinction; PTB—Permian-Triassic boundary; EP2—Early Triassic mass extinction. Lithologies as in Figure 2.

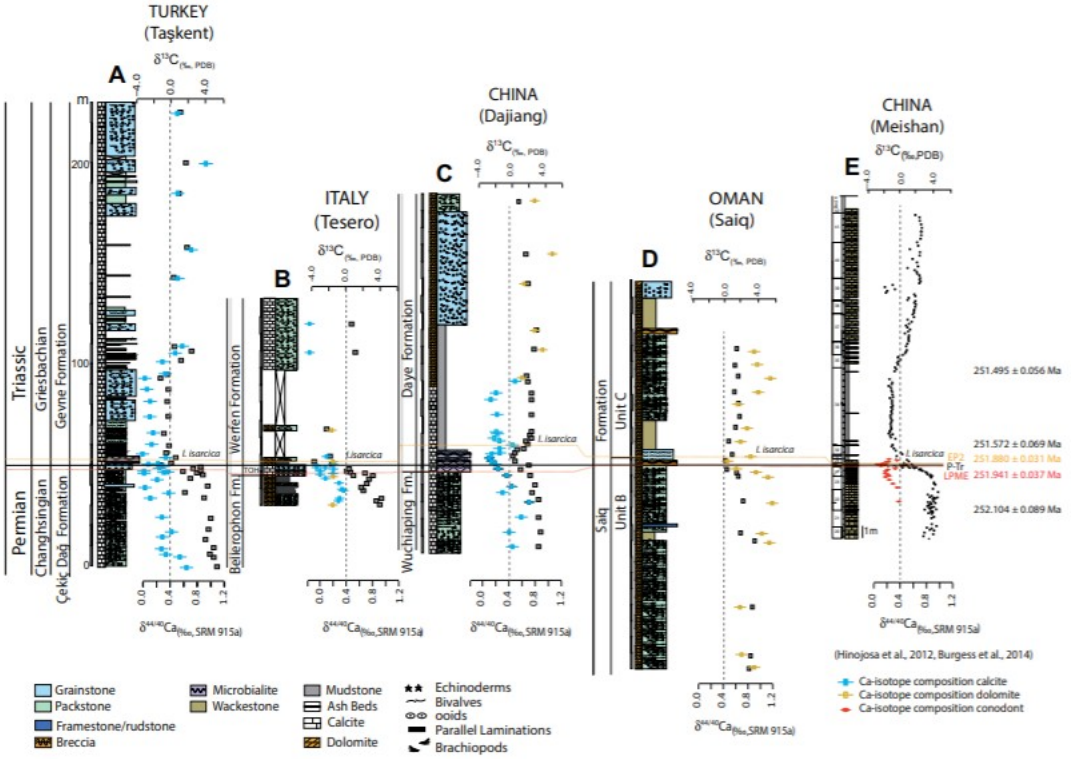

Figure 6. Carbon (dark gray squares) and calcium isotope stratigraphy of the studied carbonate successions: (A) Çekiç Dağ and Gevne Formations, Taşkent section, Taurus Mountains, southern Turkey (Lau et al., 2017); (B) Bellerophon and Werfen Formations, Tesero road section, Dolomite Mountains, NE Italy (this work; Newton et al., 2004); (C) Dajiang section, Great Bank of Guizhou (GBG), Nanpanjiang Basin, South China (Payne et al., 2010); (D) Saiq Formation, Saiq Plateau, Oman (this work); (E) Meishan section, South China (Shen et al., 2011; Hinojosa et al., 2012). Zircon U-Pb ages at Meishan are after Burgess et al. (2014). Stratigraphic locations of the end-Permian and Early Triassic mass extinction horizons are after Perri (1991), Song et al. (2012), and Richoz et al. (2010a, 2010b, 2014). EP2—Early Triassic mass extinction; P-Tr—Permian-Triassic; LPME—Late Permian mass extinction; *I.*—*Isarcicella*; PDB—Peedee belemnite.

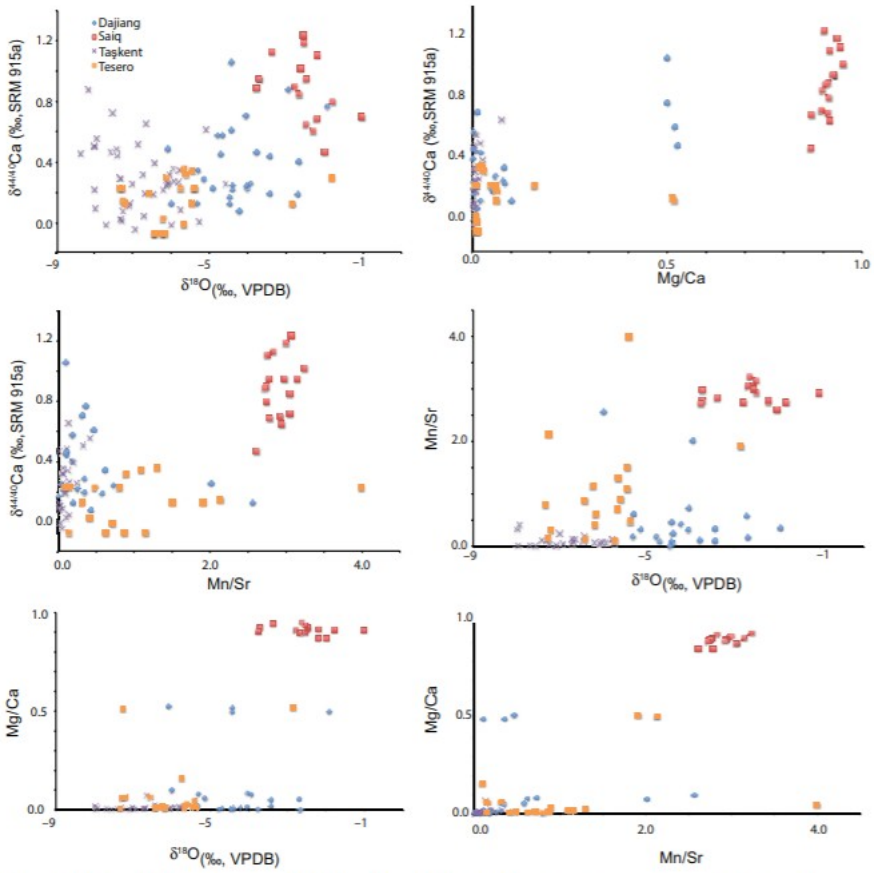

Figure 7. Scatterplots of $\delta^{44/40}$Ca and δ^{18}O values of the studied carbonate successions and elemental ratios (Mg/Ca, Mn/Sr) indicative of diagenetic alternation. Note how samples displaying higher Mg/Ca ratios display higher $\delta^{44/40}$Ca values. This suggests that the carbonate Ca isotope composition was altered due to dolomitization. VPDB—Vienna Peedee belemnite.

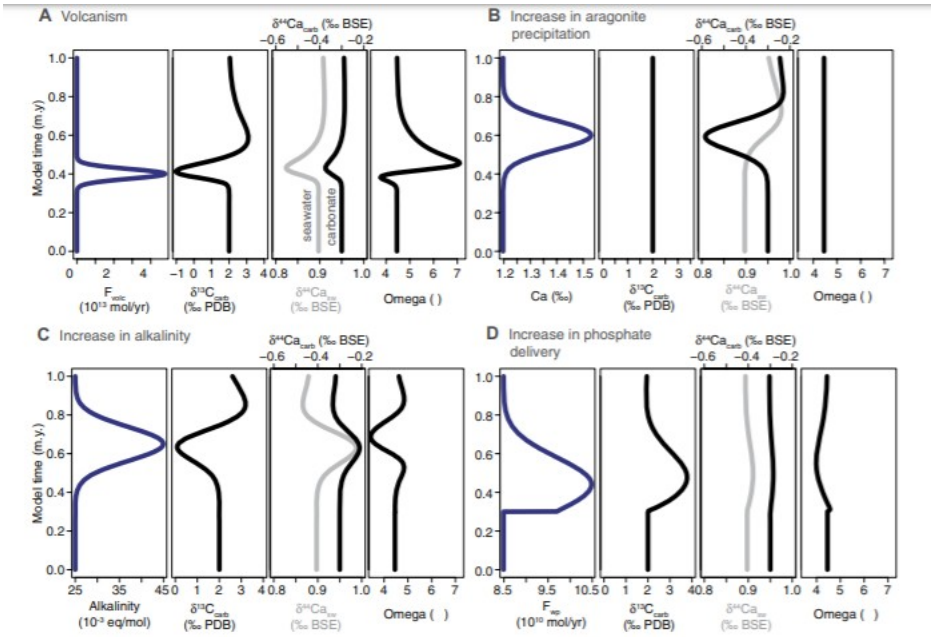

Figure 8. Box model predictions of coupled $\delta^{13}C$ and $\delta^{44/40}Ca$ in seawater (dark gray) and precipitated carbonate (black) given the following scenarios: (A) an injection of 3×10^{18} mol dissolved inorganic carbon (DIC), where $\delta^{13}C = -15‰$; (B) an increase in the proportion of primary aragonite from ~45% to 100%; (C) a 1.8-fold increase in alkalinity; and (D) an increase in organic carbon burial driven by a 1.2-fold increase in phosphate weathering. Scenarios C and D may be representative of a more widely anoxic ocean, characterized by a higher saturation state from alkalinity produced via anaerobic processes and a higher degree of productivity and organic carbon burial, respectively. The forcing mechanisms for each scenario are shown in the left-hand-most panel, and the modeled change in carbonate saturation state (Ω) can be tracked in the right-hand-most panel. In A, C, and D, the model seawater $\delta^{44/40}Ca$ results follow the same trend as the precipitated carbonate results, but following a different axis (top axis). BSE—Bulk Standard Earth; Fvolc—Flux of volcanic carbon; Fwp—Flux weathering phosphate; PDB—Peedee belemnite.

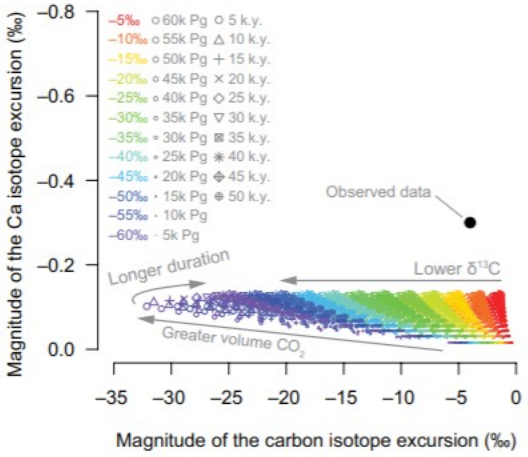

Figure 9. Comparison of modeled carbon and calcium isotope excursions under a range of input magnitudes and $\delta^{13}C$ compositions with observed excursions in $\delta^{44/40}Ca$ and $\delta^{13}C$, illustrating that while many model scenarios can account for the size of the $\delta^{13}C$ excursion, none replicates the full magnitude of the observed negative excursion in $\delta^{44/40}Ca$. For the model scenarios, symbol size reflects the magnitude of carbon addition, and symbol shape reflects the isotope composition of the added carbon.